Editorial Committee
Massimo Altarelli
Carlo J. Bocchetta
Gino D'Eliso
Stefano Fontana
Giorgio Paolucci
Franco Zanini
> http://*www.elettra.trieste.it*

Video Graphics
Giorgio Jerman

Photos
Neva Gasparo, Mario Marin

Graphic Design / Image Elaboration
Studio Link, Trieste
(Sandra Zorzetti, Rado Jagodic)
> *linkts@tin.it*

Printed by Grafiche Filacorda
Udine, 1999

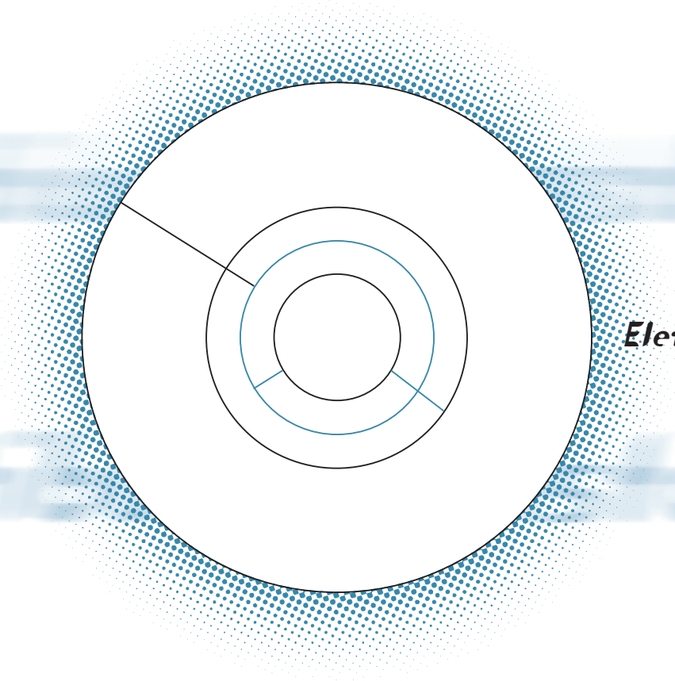

Elettra Highlights 1998-99

Contents

Preface

I am pleased to introduce the 1998-1999 edition of the Elettra Highlights. This second issue of the Highlights reports a selection of the scientific and technical achievements of the last twelve months. I hope that this relatively recent tradition will continue for many years to come.

The selected results featured here reflect the traditional points of strength of the Elettra scientific program, such as photoemission spectroscopies and microscopies, small-angle scattering, protein crystallography, and some new directions of great importance, such as surface and thin film magnetism and novel imaging techniques. The high quality of the results and the diversity of scientific disciplines concerned is something all the people working at and around Elettra, be it as members of the staff, of the associated research groups (GdR) or as users, can be proud of.

However, nothing could be more far from the truth than the description of Elettra as a mature facility, from which only “more of the same” is to be expected. There are at present no less than nine beamlines under construction, which will double the supply of beamtime by the end of 2000, and greatly extend the range of available experimental techniques. There is, in addition to the continuing effort to improve the performance and the reliability of the machine, an ambitious project to build a new injection system, with the aim of further improving the throughput. Finally, an effort is under way to improve the lot of the users also in non-technical matters, by providing comfortable and economical accomodation within walking distance fom the site.

To succeed in all these endeavours is an ambitious goal. It is obvious that it can be achieved only if Elettra continues to streamline and improve its internal organization, and, most important, to receive a strong support from the whole scientific community. This is why we pursue an even closer integration and coordination between the efforts of the Elettra and the GdR staff and a greater involvement of the users.
I hope that reading this booklet will be an enjoyable and informative experience.

Massimo Altarelli
Managing Director

Experimental Programs

INFLUENCE OF THE RADIATIVE DECAY ON THE CROSS SECTION FOR DOUBLE EXCITATIONS IN HELIUM

a u t h o r s

Jan-Erik Rubensson
Conny Såthe
(Physics Department, Uppsala, Sweden)
Stefan Cramm
Barbara Kessler
(IFF-IEE, Forschungszentrum Jülich, Germany)
Stefano Stranges
(Università La Sapienza, Roma, Italy)
Robert Richter
(Sincrotrone Trieste, Italy)
Marcello Coreno
Michele Alagia
(INFM-TASC, Trieste, Italy)

The doubly excited states of helium are fundamental for our understanding of electron correlation. Their classification is commonly based on a description of the electron correlation in hyperspherical coordinates [1]. This introduces a set of correlation quantum numbers, where the number A describes the radial correlation. For the three series converging to the threshold for ionizing the atom with the remaining electron in the N=2 level, A takes the values 1, -1 and 0.

The A=+1 wavefunction has an antinode at (or almost at) $r_1=r_2$. This is the most intense series.

The A=-1 wavefunction has node at $r_1=r_2$. This series is weaker. The wavefunctions of the A=0 states are similar to the wavefunctions of singly excited states. This is the weakest of the three series. It was discovered in the last decade. The analysis of the absorption features as resonances in the cross section for photoemission laid the foundation for the understanding of vacuum ultraviolet absorption spectra in general [2]. The theory was based on the assumption that the doubly excited states decay by autoionization and therefore interfere with the direct photoionization channel, resulting in the characteristic Fano profiles. Here we present the fluorescence yield (FY) spectrum of helium below the N=2 threshold (Fig.1).

The experiment was performed at the gas phase beamline (6.2 L). Fluorescence yield was measured perpendicular to the photon beam in the direction of the polarization. A 1000 Å polyimide filter in front of the multisphere plate detector surface ensured that the signal was unaffected by charged particles and metastable atoms. The energy calibration was obtained by simultaneously measuring the ion yield (IY). The resolution of the beamline was set to ~ 3 meV for short range scans and relaxed to ~ 7 meV for scans covering larger energy ranges.

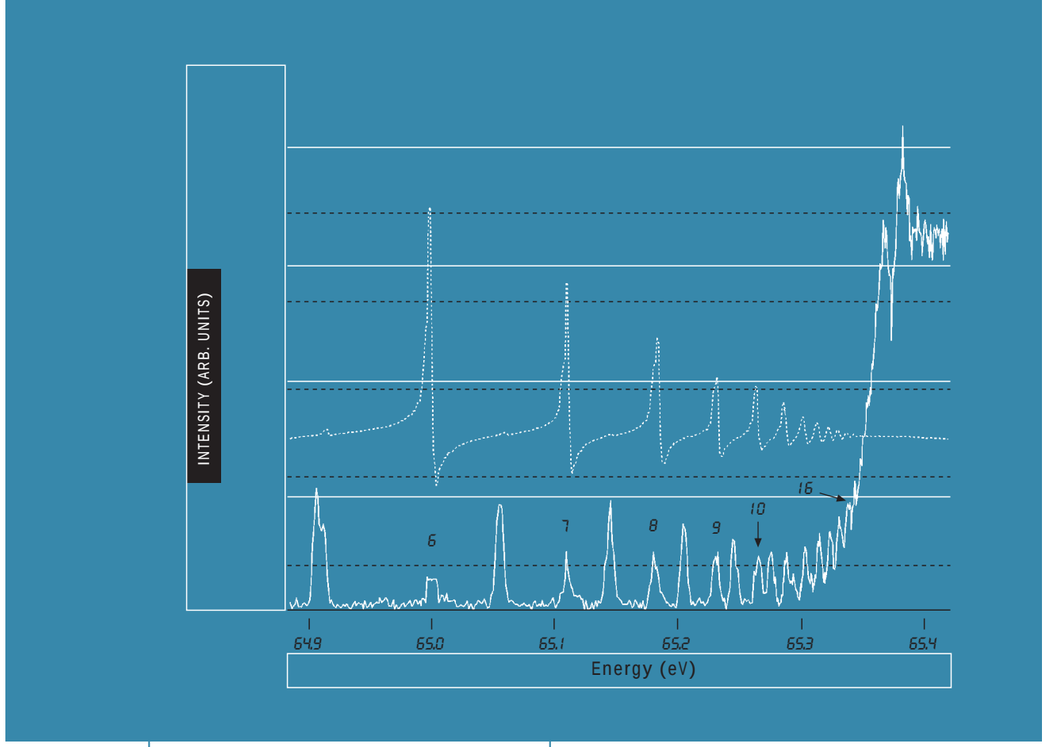

FIGURE 1

FY (full line) and IY (dashed line) spectra of the Rydberg series converging to the N=2 threshold. The numbers refer to the principle quantum number of the A=+1 series. The (n, -1) – (n-1, 0) doublets are energetically lower than the (n, +1) series.

We observe all three Rydberg series that are seen in the IY spectrum. For the lowest excitations, the FY intensity is largest for the series that are the least intense in the IY spectrum, but higher up in the Rydberg series this intensity order is reversed. It may be realized immediately that when both electrons are highly excited the overlap between them becomes smaller and therefore the autoionization decay rate decreases as we go to higher Rydberg states. Eventually, the autoionization rate must become smaller than the radiative decay rate, which is much less dependent on the electron overlap. Towards the ionization thresholds the radiative decay probability approaches unity. In a two-step model the fluorescence intensity associated with resonance *n* is: $S_n \propto \sigma_n \times \Gamma_{f,n} / (\Gamma_{f,n} + \Gamma_{a,n})$ where σ_n is the cross section for exciting the doubly excited state *n*, $\Gamma_{f,n}$ is the fluorescence decay rate, and $\Gamma_{a,n}$ is the autoionization rate. For high *n* both σ_n and $\Gamma_{a,n}$ are proportional to $(n-\delta)^{-3}$, where δ is the quantum defect. If $\Gamma_f << \Gamma_a (n-\delta)^{-3}$ the FY intensity is predicted to be independent of *n*. On approaching the ionization threshold the opposite limit will eventually be reached and we have

$S_n \sim \sigma(n-\delta)^{-3}$. Thus, a fast decrease of the FY signal will be observed if the radiative channel dominates the decay. This simple model accounts for most of the observed trends (Fig 2).

When the energy spacing between the lines approaches the resolution the overall intensity increases and we observe two maxima at 20 and 35 meV below the N=2 threshold (65.40 eV). Finally intensity drops to a constant value at the ionization limit, where the 2p - 1s transition in He^+ is observed. At n ~ 30 (around 15 meV below threshold) the splitting between the three correlated series (as determined by their quantum defect) becomes less than the (at threshold) j=1/2- j=3/2 splitting. We speculate that the FY structure dip between the peaks is due to the mixing of the three series due to spin-orbit interaction. The structure just below threshold can then not be discussed in terms of the conventional correlated models.

In conclusion, the fluorescence yield spectrum of the double excitations in helium below the N=2 threshold, reveals several new aspects of this prototype system. The radiative decay channel competes significantly with the autoionization channel. This has a profound impact on the theoretical description and the interpretation of earlier experimental results, as well as on the practice of using IY spectra as a measure for the absorption cross section [3].

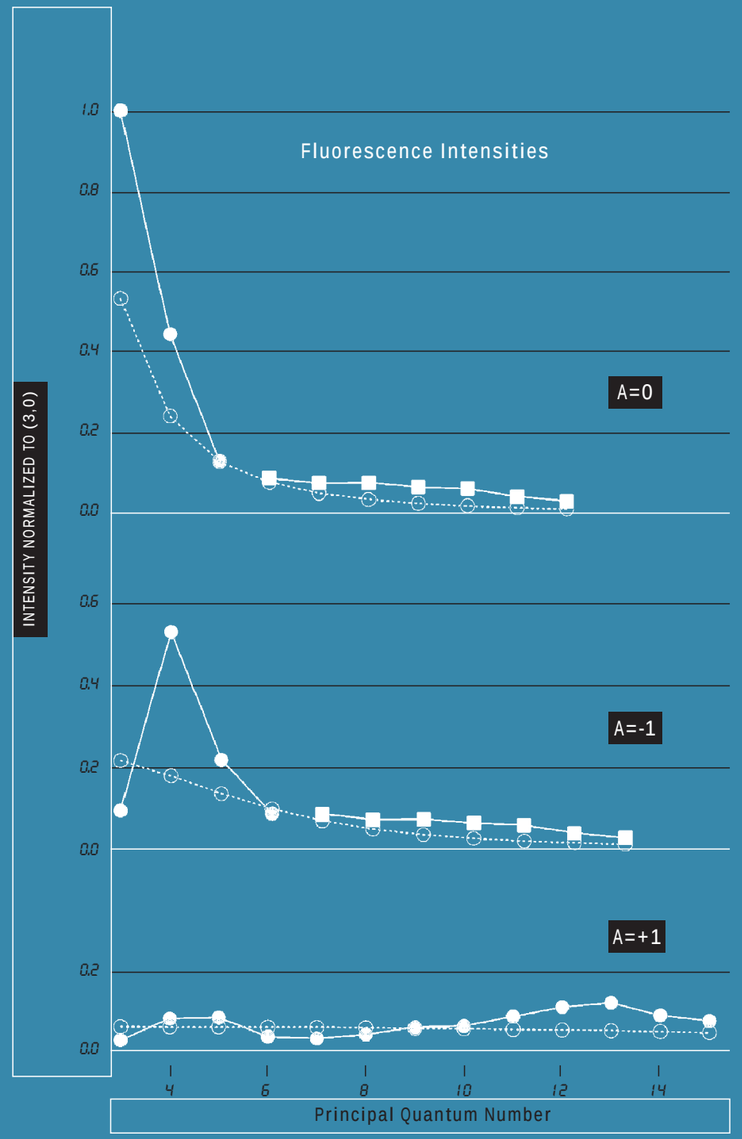

FIGURE 2

FY (filled circles) intensities for the three series normalized to (3,0), and the predictions of a simple model (open circles). The unresolved states of the A=0 and A=-1 series are plotted in both panels as filled squares.

REFERENCES [1] C. D. Lin, Phys. Rev. A. 29, 1090 (1984).
[2] U. Fano, Phys. Rev., 124, 1866 (1961). U. Fano and J. W. Cooper, Phys. Rev., 137, A1364 (1965).
[3] J.-E. Rubensson, C. Såthe, S. Cramm, B. Kessler, S. Stranges, R. Richter, M. Alagia and M. Coreno, Phys. Rev. Lett. 83, 947 (1999).

MAGNETIC ORDER AT THE RH(100) SURFACE

authors

A. Goldoni
A. Baraldi
G. Comelli
S. Lizzit
G. Paolucci
(Sincrotrone Trieste, Italy)

Two dimensional magnetic order at the Rh(100) surface is a controversial issue. Surface magnetism has been invoked by Morrison et al. [1] to explain the discrepancies between the small relaxation of the Rh(100) first intralayer spacing obtained experimentally by three independent low energy electron diffraction (LEED) studies [2] and theoretical calculations [1, 3]. By *ab initio* calculations, Morrison et al. [1] find that the first two layers of the Rh(100) surface are ferromagnetic, resulting in a 'magnetic pressure' that reduces the intralayer spacing in agreement with LEED results. This theoretical prediction of surface magnetism seems to be flawed by calculations of Weinert et al.[4] that demonstrate, in the case of Fe(001) surface, the inaccuracy of the pseudopotentials used in ref. [1]. In addition, recent first principle calculations [5] predict absence of magnetism at the Rh(100) surface. It is worth noting, however, that all these calculations are done within the local-density approximation (LDA), which does not describe properly the magnetic state. To overcome this LDA limitation, Cho and Scheffler [6] have performed a new theoretical study based on the *generalized gradient approximation*. By taking into account the vibrational contribution to the free energy for $T \neq 0$ (that was ignored in previous works), they obtained a surface relaxation in good agreement with LEED measurements [2] even without the inclusion of magnetism. Nevertheless, Cho and Scheffler show that the ferromagnetic state is practically degenerate with the non-magnetic state for magnetic moment between $0\mu_B$ and $0.6\mu_B$, suggesting that a weak ferromagnetic state can occur at the Rh(100) surface possibly stabilized by defects. This prediction agrees with spin resolved valence band photoemission measurements [7] that indicate the Rh(100) surface as weakly ferromagnetic at room temperature with a magnetic moment of $0.1\text{-}0.3\mu_B$. However, none of these predictions of magnetic phenomena at the Rh(001) surface has been verified beyond doubt so far.

Here is reported an angle resolved core level photoemission experiment of Rh(100) using linearly polarized light. For a given experimental geometry, the photoemission spectra were acquired for two opposite orientations (up and down) of the magnetic field applied parallel to the sample surface, both in chiral and non-chiral geometry. In presence of sample magnetization, this provides a series of mirror experiments for testing linear magnetic dichroism in angular distribution (LMDAD) effects [8, 9]. The experiments were carried out at the SuperEsca beamline using linearly polarized photons. The sample closed the gap of a horseshoe yoke electromagnet. The photoelectrons were collected by a 150mm hemispherical analyzer with ±1° of angular acceptance. All the photoemission spectra were acquired by keeping the sample at 100 K with an overall energy resolution better than 60 meV.

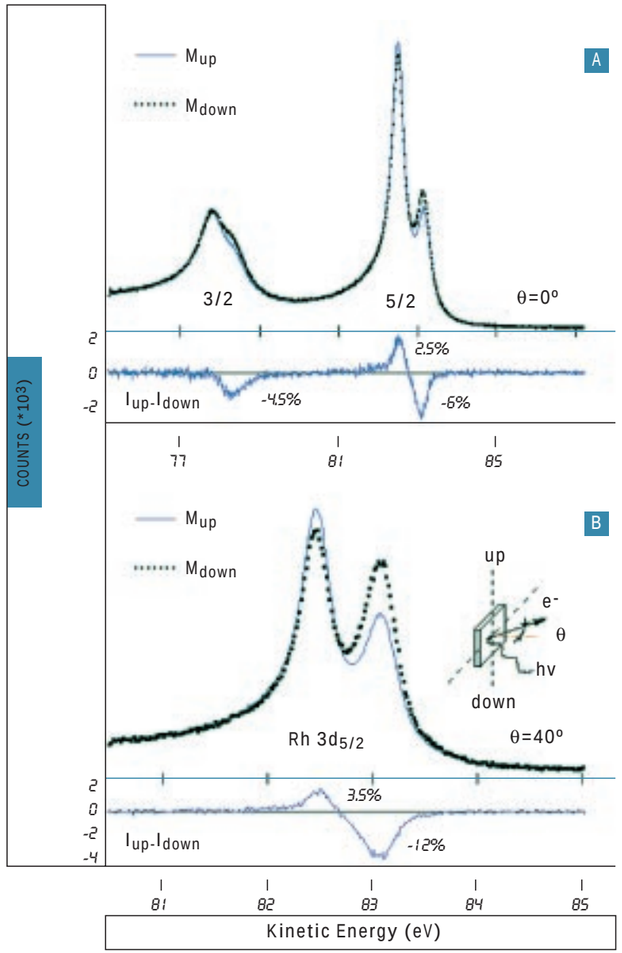

FIGURE 1

A) Rh 3d core level photoemission spectra obtained at normal emission upon reversing the magnetization from M_{up} to M_{down} in chiral geometry. B) Rh $3d_{5/2}$ core level photoemission spectra obtained at 40° of emission upon reversing the magnetization. The difference I_{up} - I_{down} is plotted in the bottom panels. The resulting peak asymmetries A, as defined in the text, are also reported.

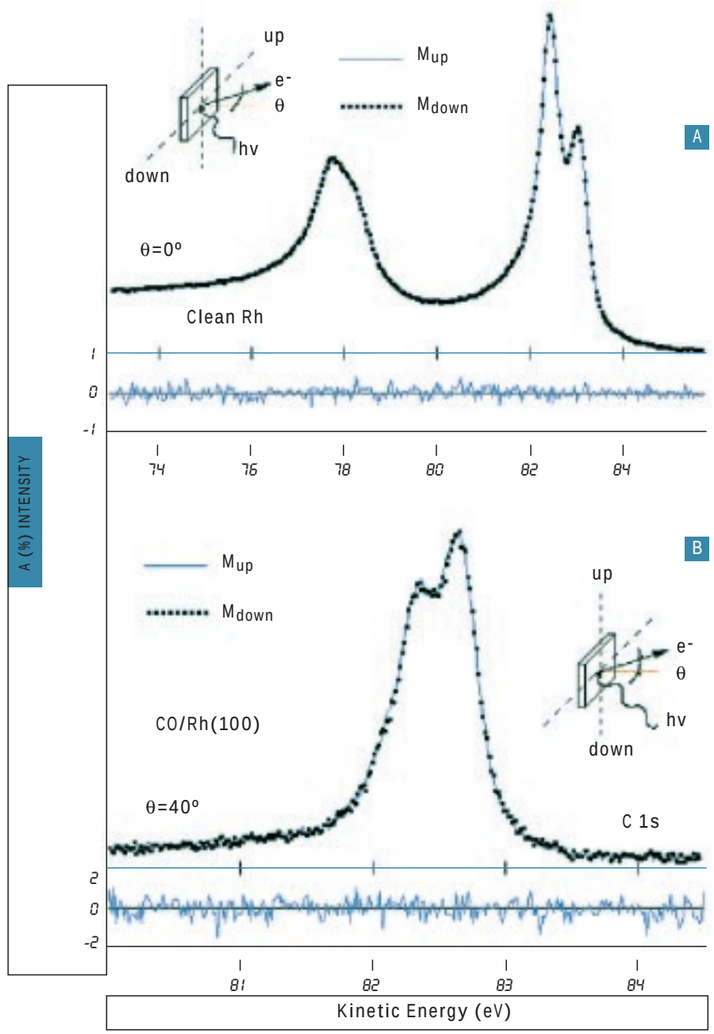

FIGURE 2

A) Rh 3d core level photoemission spectra obtained upon reversing the magnetization from M_{up} to M_{down} in non-chiral geometry, taken at normal emission. B) C 1s core level photoemission spectra of a saturation coverage of CO on Rh(100) obtained upon reversing the magnetization in chiral geometry. The bottom panels show the corresponding asymmetries.

In order to measure surface properties, we must identify surface related features in the photoemission spectra. As it is well known, the $3d_{5/2}$ core level of the Rh(100) surface presents a quite clear surface core level shifted component. The relative intensity between surface and bulk components, for a given photon energy, depends on the scattering geometry, but the surface component is always clearly visible.

By applying the magnetic field along the z-axis (i.e in the surface plane of the sample and perpendicular to the scattering plane) and reversing it by 180°, it is possible to create two mirror experiments that allow LMDAD effects in core level photoemission spectra in presence of sample magnetization [8, 9]. LMDAD can be identified by measuring the spectroscopic asymmetry A created in core level photoemission by flipping the magnetization from M_{up} to M_{down}. The asymmetry *A* is defined as:

$A = (I_{up}-I_{down})/(I_{up}+I_{down})$,

where I_{up} and I_{down} are the spectral intensities measured when the magnetic field is up or down respectively. Obviously, absence of magnetic effects implies $I_{up}=I_{down}$ and, therefore, vanishing *A*.

Fig.1 shows the Rh3d spectra taken at hν=400 eV for the two mirror geometries M_{up} (solid line) and M_{down} (points). The two spectra have been normalized at the same background intensity in the spectral regions above the $Rh3d_{3/2}$ and below the $Rh3d_{5/2}$ core levels, then an integral background has been subtracted. These spectra show clear LMDAD effects as evidenced by the asymmetry A plotted at the top of Fig. 2. The maximum asymmetry is in correspondence to the surface peak. *The surface Rh3d core levels dichroism upon reversing the magnetic field in chiral experiments indicates directly the presence of an axial symmetry induced by surface magnetization.* Being bulk Rh paramagnetic, it is worth noting that an asymmetry is also present in the region of the bulk component suggesting that the complex multiplet structure of the surface 3d peak spans over all the core level spectrum.

However, since the measurements have been performed in presence of a residual field, particular care was taken to exclude artefacts possibly related to the presence of the field. First of all, we have verified that by applying the magnetic field in the photoemission scattering plane (i.e. in a non-chiral geometry), there are not effects induced on the photoemission spectra by reversing the magnetic field. Fig. 2a shows the $3d_{3/2}$ and $3d_{5/2}$ core levels taken at normal emission, upon reversing the magnetic field in non-chiral experiments. For these spectra the asymmetry is zero, confirming the absence of LMDAD in non-chiral geometry.

To further rule out any instrumental artefact, we verified the absence of LMDAD in a sharp core level of a non-magnetic system. The latter was obtained by depositing a saturation coverage of CO molecules on the Rh(100) surface. It is established that adsorption of CO on Ni surface and Ru monolayers strongly reduce or completely quench the atomic magnetic moments, and a similar effect has been predicted in the case of adsorption on Rh monolayers [10]. In addiction, C1s emission from the CO carbon is expected to be insensitive to the presence of surface magnetization. Fig.2b shows the C1s photoemission spectra of the CO saturation coverage on Rh(100) taken upon reversing the magnetic field in chiral experiments. To avoid possible effects due to the analyzer transmission, the photon energy has been properly chosen so that the C1s electron kinetic energy might be the same as for the Rh3d photoelectrons of Fig. 1. Noteworthy, the lineshape of the two C1s photoemission spectra of Fig.2b is practically the same and no LMDAD effects are observed. The results shown in Fig.2 indicate that the observed LMDAD of the surface 3d core levels of clean Rh(100) is a genuine effect.

REFERENCES [1] I. Morrison et al., Phys. Rev. Lett. 71, 1083 (1993)
[2] PR. Watson et al., Surf. Sci. 72, 562 (1978); W. Oed et al., Surf. Sci. 207, 55 (1988); A. Begley et al., Phys. Rev. B 48, 12326 (1993)
[3] M. Methfessel et al., Phys. Rev. B 46, 4816 (1992); A. Eichler et al., Surf. Sci. 346, 300 (1996)
[4] M. Weinert et al., Phys. Rev. Lett. 71, 4097 (1993)
[5] S.K. Nayak et al., Phys. Rev. B 56, 8849 (1997)
[6] J.-H. Cho and M. Scheffler, Phys. Rev. Lett. 78, 1299 (1997)
[7] S.C. Wu et al., Phys. Rev. B 49, 14081 (1994)
[8] Ch. Roth et al., Phys. Rev. Lett. 70, 3479 (1993); G. Rossi et al., Solid State Commun. 90, 557 (1994); G. Rossi et al., NATO ASI series B: Physics 345, 181 (1995)
[9] B.T. Thole and G. van der Laan, Phys. Rev. B 49, 9613 (1994); G. van der Laan, NATO ASI series B: Physics 345, 153 (1995)
[10] C.S. Feigerle et al., Phys. Rev. Lett. 56, 2207 (1986); PW. Selwood, Chemisorption and Magnetism *(Academic Press, New York, 1975); P. Pfandzetter et al., Phys. Rev. Lett. 74, 3467 (1995); K.C. Hass et al., Phys. Rev. B 53, 44 (1996)*

PHASE TRANSITION AND INEQUIVALENT CARBON ATOMS IN K_3C_{60} (111)

authors

A. Goldoni
G. Comelli*
G. Paolucci
(Sincrotrone Trieste, Italy)
L. Sangaletti
F. Parmigiani
(INFM - Dipartimento di Matematica e Fisica dell' Università Cattolica, Brescia, Italy)
S.L. Friedmann
Z.-X. Shen
(Department of Applied Physics and Center for Material Research, Stanford University, California)
M. Peloi
*(Laboratorio TASC-INFM, Trieste, Italy)

In the stable A_3C_{60} compounds (where A indicates an alkali metal or a binary composition of alkali metals) the fullerene balls form a *fcc* lattice, while the alkali metal atoms are intercalated in the octahedral and tetrahedral interstitial sites [1-3]. Because of the reduced symmetry induced by the cubic crystal field, the carbon atoms of the fullerene cage result into three non-equivalent atomic coordinations, namely C1, C2 and C3, with a stoichiometric ratio of 1:2:2. The distortion of the molecular structure, due to the interaction with alkali metals, can enhance this dissimilarity. Theoretical predictions suggest, also for pure C_{60}, an inhomogeneity of the charge distribution over the three non-equivalent carbon sites [4]. This effect is enhanced in highly ordered systems where an electronic charge transfer to C_{60} occurs. Another important issue in describing the physical properties of these compounds is the orientational motion of the C_{60} molecules [5-7]. It has been shown that in A_3C_{60} the C_{60} molecules cannot rotate almost freely as in the pure C_{60} solid [1,2]. X-ray diffraction [2] (XRD) data at room temperature indicate that the molecules can randomly assume two orientations related by a 90° rotation about the twofold <100> axes. Nuclear magnetic resonance (NMR) experiments [5-7] suggest that the molecules can twist back and forth between the two possible orientations (uniaxial motion) and can occasionally flip [7] to a perpendicular rotational axis (perpendicular motion). By reducing the temperature, the molecular motions are gradually slowed down. Related to this, a phase transition at T*=200K has been claimed for K_3C_{60} on the basis of NMR

data [5], although no evidence for structural changes has been found yet by XRD [3]. It has been suggested that the slowing down of the molecular motions at low temperature, as well as the occurrence of the phase transition at 200K, could modify the electronic structure in such a solid with respect to the high temperature case [5,7]. An experimental observation of these effects by core level spectroscopies may clarify the correlation of the molecular motion and charge inhomogeneity with the anomalous normal state properties of A_3C_{60} fullerides and with the changes in the density of states at the Fermi edge (EF) which accompanies the superconductivity.

High resolution synchrotron radiation photoemission (XPS) and absorption (XAS) spectroscopies from the C1s core level performed at the SuperESCA beamline, were used to investigate a K_3C_{60}(111) single phase ordered film as a function of temperature [8]. Fig.1 shows the C*1s* XPS spectra of the single-phase K_3C_{60} ordered film measured at 600K and 30K (top spectra). The modification of the C*1s* core level between 600K and 30K is evident. When the temperature is reduced from 600K to 30K the K_3C_{60} C*1s* core level splits in at least two components becoming broader, with part of the spectral weight moved to higher and lower binding energies. To confirm this effect, the C*1s* XPS spectra of K_3C_{60} are compared to those measured from a K_4C_{60} single-phase film (*bct* structure) under the same experimental conditions (bottom spectra). The K_4C_{60} single-phase film was obtained by annealing the K_3C_{60} single-phase film at 750K for 36 hours in UHV [9]. Two effects are clearly visible: 1) the K_4C_{60} C*1s* XPS spectra are much sharper than those measured on K_3C_{60}; 2) they show an opposite temperature dependence with respect to the K_3C_{60} spectra, i.e. they shrink as the temperature is decreased because of the reduced phonon population. This indicates that the broadening and the splitting observed in the K_3C_{60} spectra are not artefacts due to the low temperature absorption of different carbon species, e.g. residual gases, but are genuine effects related to K_3C_{60}.

The inset of Fig.1 shows the temperature dependence of the FWHM of the C*1s* photoemission peak of K_3C_{60}, as measured on the raw data. Two anomalies are clearly present at 400K and 200K. We focus first on the jump at 200K that well corresponds to the abrupt increase of the ^{13}C NMR line at the same temperature [5]. The ^{13}C FWHM has, indeed, a clear jump at 200K in correspondence to the claimed phase transition, and its temperature dependence looks like that of the C*1s* FWHM in the range 25K – 400K [5]. Therefore, Fig. 1 shows that the gradual slowing down of the molecular motions modifies the line shape of the C*1s* core level. Below 200K the C*1s* core level clearly reveals the presence of several chemically shifted components, while at 600K it appears as a narrower single line emission. Fig. 2a shows that a fit based on a model with three non-equivalent carbon atoms per molecule is able to satisfactory reproduce the C*1s* core level lineshape at 30 K. The relative weight of the components is close to 1:2:2. Further support to this interpretation comes from the XAS data of Fig. 2b, where the energy position and width (sharper than the C*1s* total width in XPS) of the first absorption peak is consistent with the presence of chemically shifted components in the XPS spectrum. These findings, in agreement with the theoretical prediction [4], can be related to chemically inequivalent carbon atoms having different valence charge distribution.

Moreover, the evolution with temperature of the XPS C*1s* core level confirms the presence of a sudden change at 200K, in agreement with NMR data, probably associated to an ordering of the rotation-

FIGURE 1

C1s core level of K_3C_{60} and K_4C_{60} at two different temperatures. Inset: temperature dependence of the C 1s FWHM for K_3C_{60}.

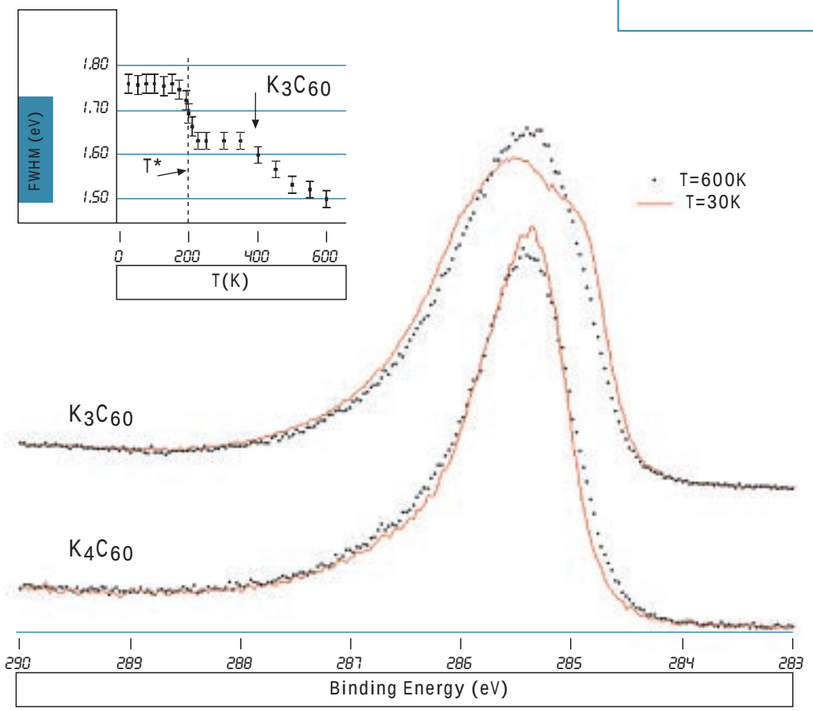

al axis [5]. It also suggests that above 400K the fast molecular motion affects the electronic structure of K_3C_{60} reducing the chemical shifts by partially averaging the charge distribution inhomogeneity over the carbon sites. A model based on the inhomogeneity of the conduction electron distribution at the molecular level, which tentatively explains these results and the NMR observations, has been proposed and discussed elsewhere [8].

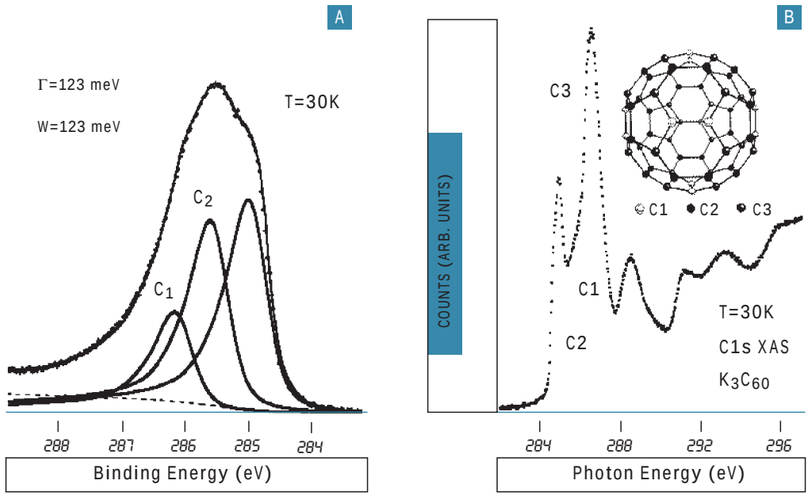

FIGURE 2

A) Best fit of the C1s core level spectrum of K_3C_{60} at 30K.
B) XAS spectrum of K_3C_{60}.
Inset: The three inequivalent carbon atoms of the C_{60} molecule in K_3C_{60}.

REFERENCES [1] R.C. Haddon et al., Nature 350, 320 (1991)
[2] P.W. Stephens et al., Nature 351, 632 (1991)
[3] G.M. Bendele, P.W. Stephens and J.E. Fischer, in Fullerenes and Fullerene Nanostructures, *edited by H. Kuzmany, J. Fink, M. Mehring and S. Roth, 142 (World Scientific, 1996)*
[4] S. Saito and A. Oshiyama, Phys. Rev. Lett. 66, 2637 (1991); D.L. Novikov, V.A. Gubanov and A.J. Freeman, Physica C 191, 399 (1992); W. Andreoni, P. Giannozzi and M. Parrinello, Phys. Rev. B 51, 2087 (1995)
[5] Y. Yoshinari et al., Phys. Rev. Lett. 71, 2413 (1993); Y. Yoshinari et al., Phys. Rev. B 54, 6155 (1996)
[6] R. Tycko et al., Phys. Rev. Lett. 68, 1912 (1992); S.E. Barret and R. Tycko, Phys. Rev. Lett. 69, 3754 (1992)
[7] K. Holczer, Int. J. Modern Phys. B 6, 3967 (1992); K. Holczer et al., Europhys. Lett. 23, 63 (1993)
[8] A. Goldoni et al., Phys. Rev. B 59, 16071 (1999)
[9] D.M. Poirier, Appl. Phys. Lett. 64, 1356 (1994)

SB-TERMINATED SI(100), SI(110) AND SI(111) SURFACES STUDIED WITH HIGH RESOLUTION CORE-LEVEL SPECTROSCOPY

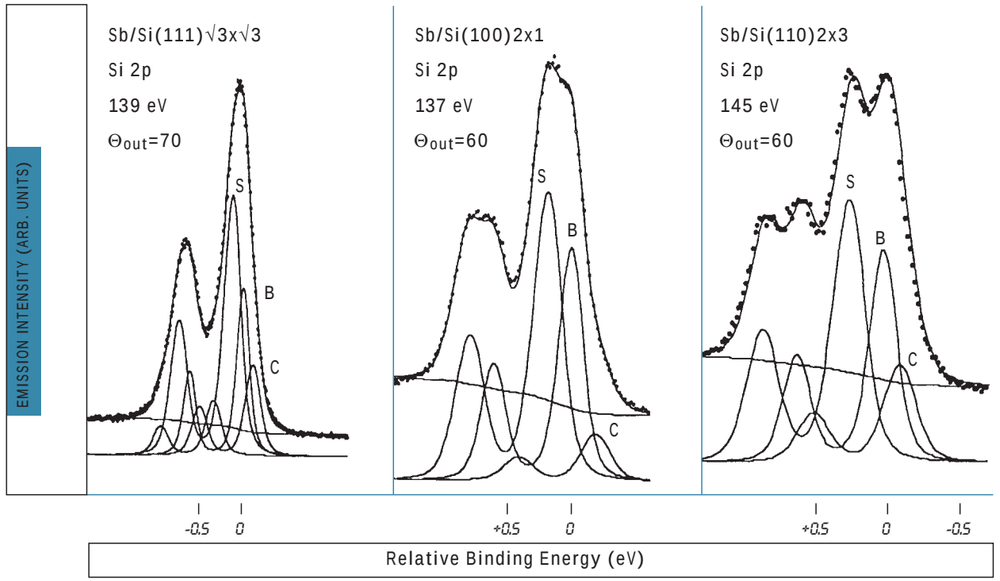

a u t h o r s

A. Cricenti
C. Ottaviani
C. Comicioli
C. Crotti
L. Ferrari
C. Quaresima
P. Perfetti
(Istituto di Struttura della Materia, CNR, Rome, Italy)
G. Le Lay
(CRMC2, UPR CNRS 7251, Campus de Luminy, France)

The interaction of Antimony with Si surfaces is of great interest since Sb is an important dopant material used in Si molecular beam epitaxy and is used as a surfactant for Ge/Si heterostructures

Core-level spectroscopy was extensively used to study clean and Sb terminated Si(100), Si(110) and Si(111) surfaces with some controversial results due to the limited energy resolution. The Sb terminated Si(100) and Si(111) surfaces were thought to be ideal bulk terminated since no surface component was observed in the Si 2p core level.

We report on synchrotron radiation photoelectron spectroscopy studies performed on the high energy resolution VUV beam line at ELETTRA in Trieste of the Si 2p core levels obtained with very high resolution from Sb overlay-

ers onto the low index silicon surfaces Si(100) [1], Si(110) [2] and Si(111) [3]. The improved energy resolution of third generation synchrotron radiation facilities has shown the presence of a strong interfacial component shifted 0.2, 0.24 and 0.13 eV , respectively, on the high binding energy side respect to the bulk peak (see fig. 1). Such surface contributions are, mainly, ascribed to charge transfer between the metal and the topmost silicon atoms. A small component is always present on the high kinetic energy side and is suggested to be due to contribution from defects. The Sb 4d core-level spectrum (fig. 2) is well represented by one doublet, characteristic of Sb atoms adsorbed in a unique environment.

On the Si 2p core level of a Sb/Si(111) surface [3] taken in bulk sensitive mode (fig. 3), we found a very narrow bulk component with a total full width half maximum (FWHM) of 130 meV (100 meV Gaussian FWHM), that yields an upper limit of 70 meV for phonon broadening and inohomogenities contribution at T=100 K. A value of 90 meV is derived for the surface component.

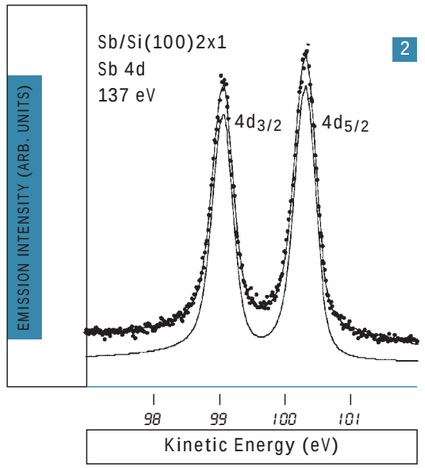

2

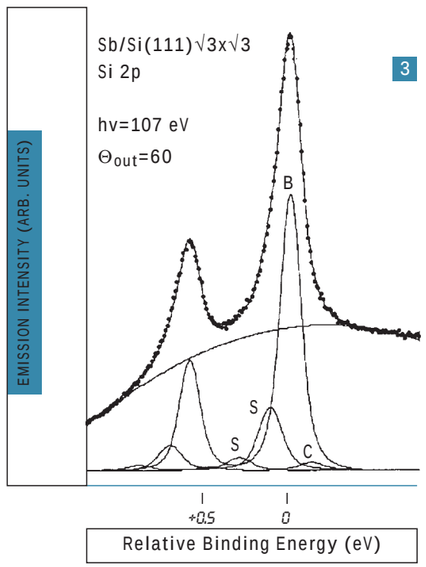

3

REFERENCES [1] High resolution Si 2p core-level photoemission spectroscopy on Sb terminated Si(100) surface: evidence for a strong interfacial component. A.Cricenti, P.Perfetti, G. Le Lay, Surf. Sci. 401, 427 (1998)

[2] Sb/Si(110)2x3 surface studied by high resolution Si 2p core-level photoemission spectroscopy A. Cricenti, C. Ottaviani, C. Comicioli, P.Perfetti, G. Le Lay, Phys. Rev. B 58, 7086 (1998).

[3] Charge transfer and phonon broadening at a Sb/Si(111)√3x√3 surface by high resolution Si 2p core-level. A. Cricenti, C. Quaresima, C. Ottaviani, L. Ferrari, P. Perfetti, C. Crotti, G. Le Lay, submitted to Phys. Rev. Lett.

IN SITU OBSERVATION OF A SURFACE CHEMICAL REACTION BY FAST X-RAY PHOTOELECTRON SPECTROSCOPY

authors

Adam F. Lee
Karen Wilson
Ruth L. Middleton
Richard M. Lambert
(Department of Chemistry, University of Cambridge, England)
Andrea Goldoni
Giorgio Paolucci
Alessandro Baraldi
(Sincrotrone Trieste, Italy)

Background

The introduction of modern surface science techniques has led to rapid advances in our understanding of chemical phenomena occurring at the solid-gas interface, impacting in particular on heterogeneous catalysis. However the development of new catalytic materials still proceeds by largely empirical methodologies. In part, this reflects the dearth of quantitative methods for identifying surface species as they are formed and consumed during reaction. Here we demonstrate the first use of time-resolved fast X-ray photoelectron spectroscopy as a chemically specific, quantitative probe in a study of the trimerisation of ethyne to benzene over a catalytically active Pd(111) surface. We have measured the threshold temperature and activation barrier for trimerisation, and elucidated details of the reaction pathway and associated configurational changes in the adsorbed layer. Our findings demonstrate the general utility of fast XPS for *in situ* studies of complex surface chemical phenomena.

Results

Fast XPS data showed that at 100 K ethyne adsorbs on Pd(111) *via* a precursor state into a chemisorbed species whose C-C axis lies parallel to the metal surface (NEXAFS). Temperature-programmed C 1s XP spectra resulting from heating C_2H_2 exhibit large temperature-dependent binding energy shifts and variations in peak, due to changes in both the chemical state and number density of adsorbed hydrocarbon species. Using comparative C 1s spectra obtained during the low temperature chemisorption of benzene overlayers on Pd(111), all spectra could be fitted by 3 components centred at 288.88, 289.54 and 289.01 eV. The sequence in which these components are populated allows their assignment

as unreacted ethyne, strongly chemisorbed flat-lying benzene, and weakly bound tilted benzene respectively. The temperature-dependent intensity variations of these components, and their sum (after correction for relative photon excitation cross-sections) are shown in the figure. We can follow the evolution of the reactingsystem in which the first product to appear is flat-lying benzene; this is followed by formation of tilted benzene part of which desorbs and part of which converts to flat benzene as the temperature is raised and the surface depleted of adsorbate. At still higher temperatures, adsorbed phenyl species are formed which disproportionate to gaseous benzene and adsorbed carbon. We deduced an activation energy of ~4.8 kJ mol^{-1} for the conversion of chemisorbed ethyne to flat-lying benzene. Our observations provide the first direct evidence that surface reactions are not rate limiting for appearance of the gaseous benzene product: the desorption step is rate limiting. They also demonstrate that important configurational changes occur in the adsorbed product as the reaction proceeds. These changes are critically important in determining the kinetics of the overall reaction. Kinetic control can be achieved by designing the catalyst surface (e.g. by alloying Pd with Au) so as to favour the formation of tilted benzene thus maximising activity and optimising selectivity.

FIGURE 1

C 1s intensities showing evolution of surface species as reaction proceeds.

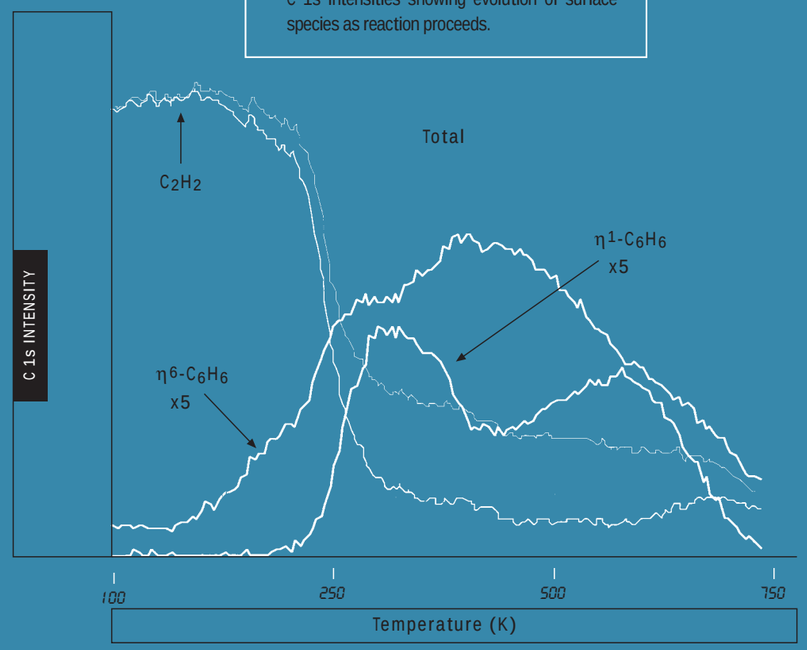

ELECTROCHEMICAL PROMOTION OF HETEROGENEOUSLY CATALYSED REACTIONS

authors

Mintcho Tikhov
Alejandra Palermo
Federico Williams
Samuel Tracey
Richard Lambert
(Department of Chemistry, University of Cambridge, England)
Maya Kiskinova
Sebastian Gunter
Luca Gregoratti
(Sincrotrone Trieste, Italy)

Background

Electrochemical promotion (EP) is a unique way of achieving *in situ* control of catalyst performance: activity and selectivity can be varied in a reversible and controlled way while the catalyst is actually working in a reactive atmosphere. This phenomenon occurs when catalytic reactions take place on a metal film that is supported on a solid electrolyte. By varying the catalyst potential (measured with respect to a reference electrode) one can induce large, reversible changes in catalyst activity and selectivity. These changes are thought to be caused by electro-pumped promoter species (e.g. Na) which spill-over from the solid electrolyte onto the catalytically active metal film. Our motivation is threefold (i) to understand the phenomenon at the microscopic level (ii) to use EP in order to determine the mechanisms of catalytic reactions (iii) to broaden the applicability of the technique and to exploit it in the design of new catalytic systems.

Results

We carried out a detailed study of the several EP systems at the ESCA microscopy beamline using Na or K-β" alumina as the solid electrolyte and pumping Na or K to Cu, Pd and Pt surfaces. Nothing like this has been done before. By combining XPS and spatially resolved XPS we showed unambiguously the nature of the processes involved. Electrochemically induced changes in catalyst potential over a range of ~ 1V are correlated with the spillover of the electro-pumped promoted species (e.g. Na or K) from the solid electrolyte to the surface of the porous metal

FIGURE 1

Na2p grazing emission XPS showing the effect of catalyst potential (V_{WR}) in pumping sodium to/from the Cu film under UHV conditions at 523K

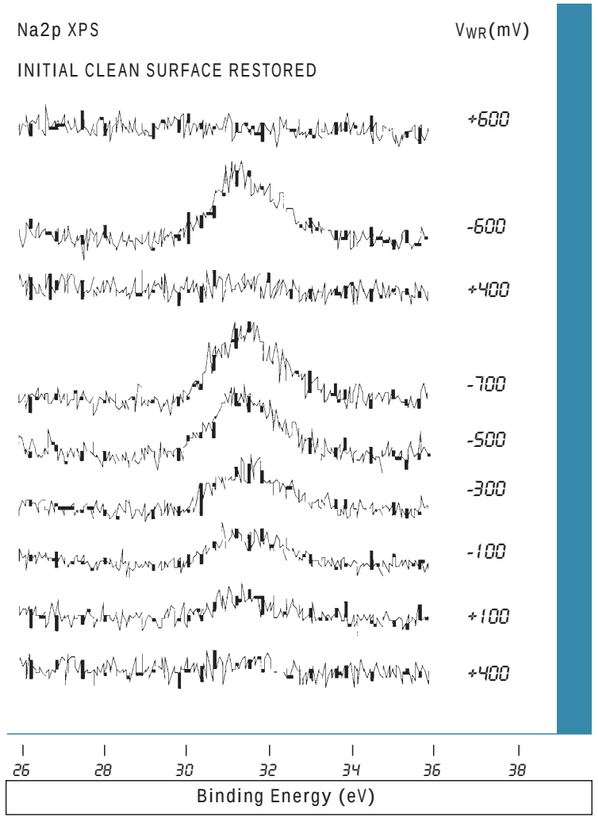

film. From the measured XPS intensities we were able to determine for the first time the relation between catalyst potential and the alkali promoter coverage. Moreover, we showed that the spillover phenomenon, directly imaged by XPS microscopy, occurs on a time scale of seconds and that defects and pores in the metal film act as sources (or sinks) for the electropumped promoter species. We also show that the effect of catalyst potential on alkali promoter coverage is indeed completely reversible, in good accord with the catalytic results.

CHEMICALLY RESOLVED *IN SITU* IMAGING OF CHEMICAL WAVES IN CATALYTIC NO REDUCTION WITH HYDROGEN ON RH(110)

authors

A. Schaak
E. Schütz
M. Hinz
R. Imbihl
(Institut für Physikalische Chemie und Elektrochemie, Universität Hannover, Germany)
S. Günther
F. Esch
M. Marsi
M. Kiskinova
(Sincrotrone Trieste, Italy)

Chemical wave patterns in catalytic surface reactions have been an area of intense research in recent years [1]. The main method with which these patterns have been imaged is photoelectron emission microscopy (PEEM). This method images primarily the work function but yields no or only very indirect information about the chemical identity of the imaged species. With PEEM a number of unusual wave patterns have been observed in the NO + H_2 reaction on Rh(110): rectangularly shaped target patterns and spiral waves and isolated traveling wave fragments have all been seen [2]. The unusual types of patterns have been attributed to the presence of different N- and O-induced reconstructions with different diffusion anisotropies [3]. In order to obtain chemically resolved images of wave patterns an *in situ* imaging with scanning photoelectron microscopy (SPEM) was conducted at the electron storage ring ELETTRA [4]. Wave patterns in the NO + H_2 reaction on Rh(110) were adjusted under isothermal conditions in the 10^{-7} mbar range operating the UHV chamber as a continuous flow reactor. Figure 1 displays elementally resolved images of a pulse train propagating from left to right. Pulse velocities are ca. 0.5 µm/s. In each single pulse the oxygen is completely reacted away and replaced by a nitrogen overlayer (not shown here). The Rh 3d peak experiences a small shift of 0.1 eV to higher binding energy (BE) when the surface is oxygen covered. This allowed us to monitor the lateral variation in the chemical state of Rh by tuning to the lower or higher BE side of the peak during rastering. From the XPS intensities absolute coverages were obtained by calibrating the XPS peaks in Fig. 2 with LEED

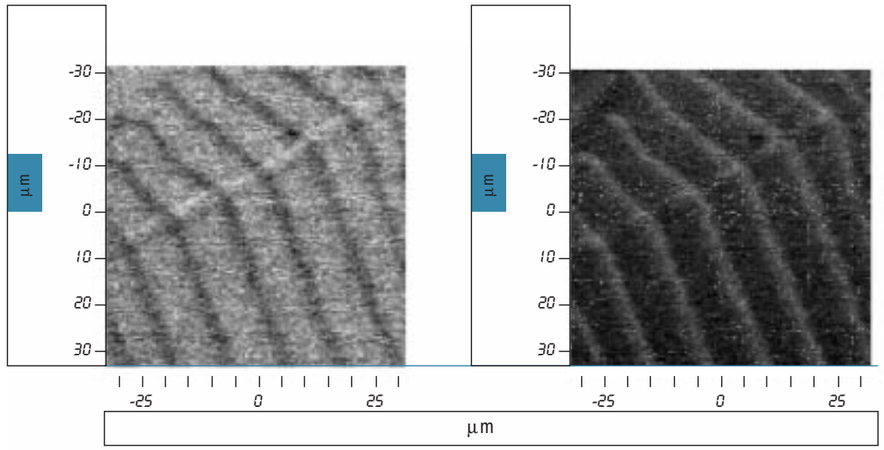

structures of known coverages, i. e, a c(2x6)-O with θ_O=0.66 and a (2x1)-N with θ_N=0.5 [3].
From these measurements a concentration profile for a single pulse could be constructed reproduced in Fig. 2. Starting from the oxygen covered surface with a c(2x6)-O (θ_O=0.66), oxygen is reactively removed by hydrogen and replaced by a (2x1)-N (θ_N=0.5) nitrogen overlayer. On this (2x1)-N surface NO can still adsorb and dissociate so that an increasing coverage of coadsorbed oxygen destabilizes the nitrogen which finally desorbs thus reestablishing the initial state of an oxygen covered surface. From the information gained in the SPEM experiments a realistic mathematical model was developed which contains no arbitrary assumptions and which successfully reproduces the experimental results [4].

FIGURE 1

Elemental maps recorded with SPEM showing propagating pulse trains in the system Rh(110)/NO + H_2.
Experimental conditions: T= 530 K, p_{NO}=1.7x10^{-7} mbar, pH_2=6.4x10^{-7} mbar, photon energy 625.7 eV.

REFERENCES [1] R. Imbihl, G. Ertl, Chem. Rev. 95, 697 (1995).
[2] F. Mertens, R. Imbihl, Nature 370, 124 (1994).
[3] M. Kiskinova, Chem. Rev. 96, 1431 (1996); G. Comelli, V. R. Dhanak, M. Kiskinova, K. C. Prince, and R. Rosei, Surf. Sci. Rep. 32, 165 (1998).
[4] A. Schaak, S. Günther, F. Esch, E. Schütz, M. Hinz, M. Marsi, M. Kiskinova and R. Imbihl, Phys. Rev. Lett. 83, 1882 (1999).

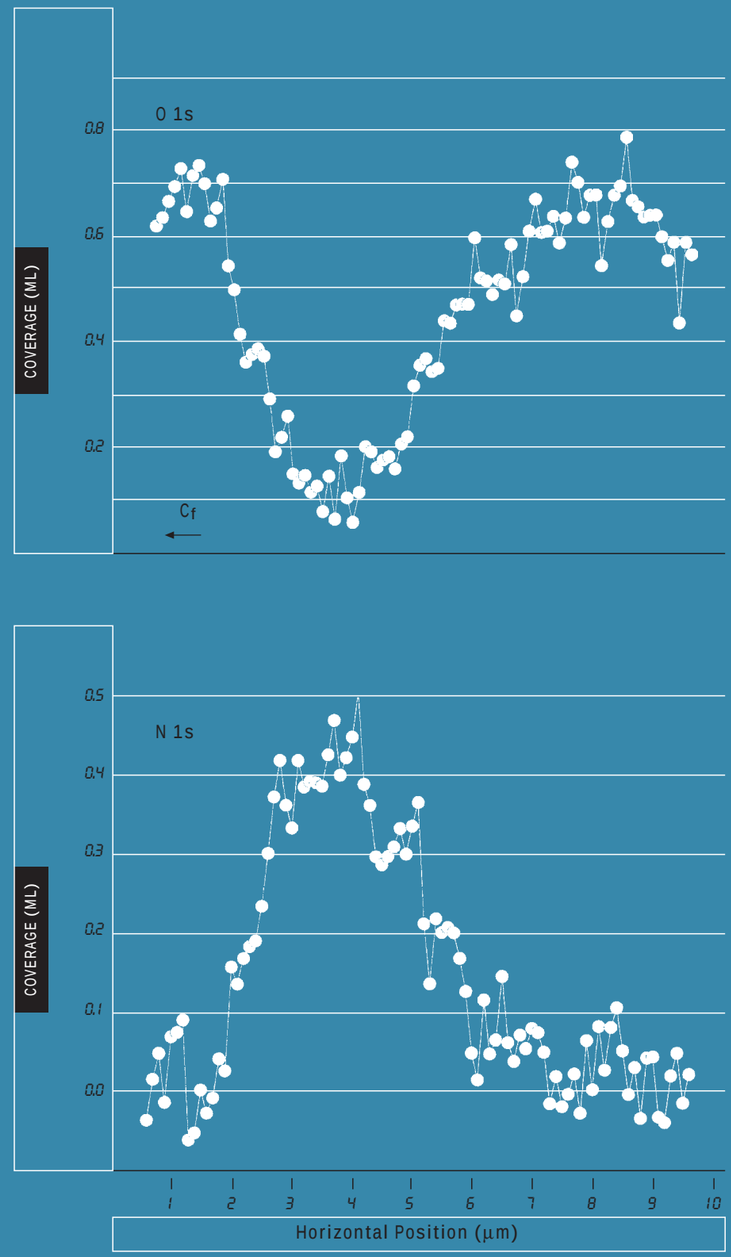

FIGURE 2 Experimentally determined concentration profile for a single pulse.

HIGH RESOLUTION PHOTOEMISSION AT THE C(2X2) SI-CU(110) SURFACE ALLOY

authors

C. Rojas
F.J. Palomares
E.Román
J.A. Martín-Gago
(Instituto Ciencia de Materiales de Madrid-CSIC, Spain)
M.F. López
(Centro Nacional de Investigaciones Metalurgicas, Madrid, Spain)
A. Goldoni
G. Paolucci
(Sincrotrone Trieste, Italy)

In the last decade the formation of two-dimensional (2D) surface alloys has attracted much attention. The possibility of forming stable surface phases unmiscible in the bulk, characterized by different physical properties, has opened a new field of research. Most of the known 2D alloys are formed by bimetallic elements. However, we have recently reported on the existence of a surface alloy formed by room temperature deposition of 0.5 Si monolayers (ML) on a Cu(110) surface[1,2,3]. The high degree of crystallographic order of the surface alloy may be of great importance in testing the fundamental properties of the Schottky barrier formation and the semiconductor-on-metal interface bonding.

We have determined the geometrical structure of the 2D Si-Cu(110) surface alloy by synchrotron radiation X-ray photoelectron diffraction at the Super-ESCA beam line in ELETTRA. Thus, by comparing XPD scans recorded at different photon energies with Single Scattering Cluster (SSC) and Multiple Scattering calculations, we have found that the geometrical structure of the alloy consists of an alternative replacement of the Cu surface atoms of the [1$\underline{1}$0] rows by the deposited Si atoms, forming a c(2x2) superstructure. The atomic structure is schematically represented in the upper part of fig. 1. The Si atoms have been found to be inward relaxed, around 0.25 Å, with respect to the surface Cu atoms [1,2,3].

Fig. 1 shows the high resolution Si 2p core level photoemission spectra of the c(2x2) surface alloy at 100K (upper curve) and at room temperature (lower curve). By a visual inspection of the low temperature spectrum, without any further decomposition, 4 different components with their corresponding spin-orbit contribution, can be observed. We would like to remark that , as far as we know, this is the narrowest Si2p core level peak in solid state ever reported. The Full Width at Half Maximum of the peak is 150 meV, indicating both, the high degree of order of the Si atoms in the alloy and the high resolution of the Super-ESCA beam line.

In the geometrical model of fig.1 can be appreciated that the chemical environment of the Si atoms in this c(2x2) structure is the same for all the Si atoms at the surface, however, up to four different components can be univocally separated in the Si2p photoemission spectra of fig. 1. In order to know the atomic origin of these components, we have combined photoemission spectroscopy and photoelectron diffraction (XPD) with STM images recorded at our home laboratory [4].

We have recorded XPD azimuthal scans for every component of the Si2p spectrum. Thus, the local environment of the emitting Si atoms can be examined. Fig. 2 shows az-

STRUCTURAL MODEL

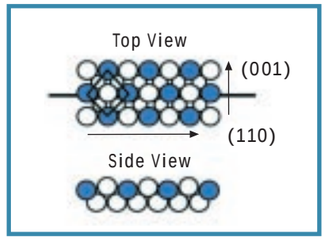

Schematic representation of the structural model for the c(2x2) Si/Cu(110) surface alloy indicating the unit cell and main surface directions. Filled circles represent Si atoms and empty circles Cu atoms.

FIGURE 1

Si2p core level photoemission spectrum of the c(2x2) Si/Cu(110) surface alloy recorded at 120K and at 300K. The curves at the bottom of every spectrum represent the different components, Si1,Si2, Si3 and Si4. The overall fit is represented by the solid line overlapping the experimental data points

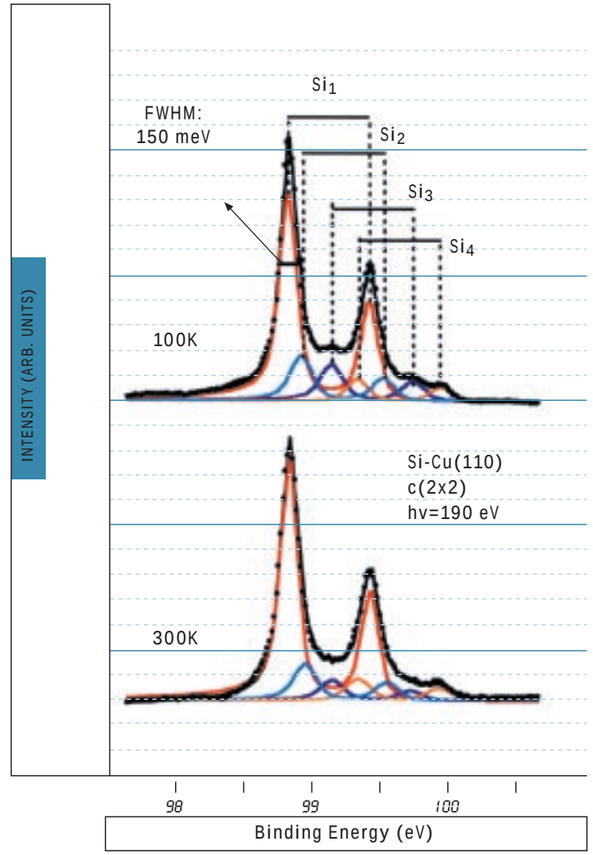

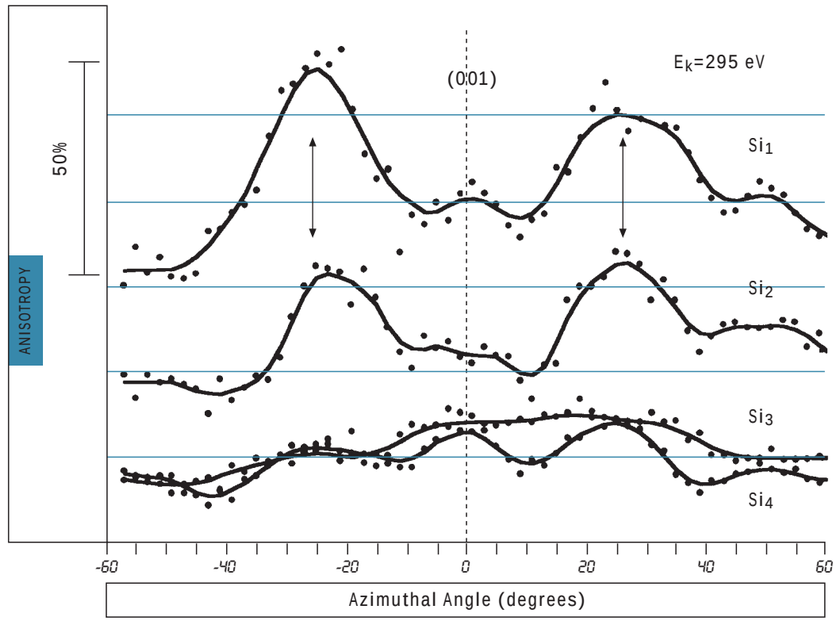

imuthal scans recorded at a polar angle of 72 degrees with respect to the surface normal. Analogous scans have been obtained and analysed for different kinetic energies and surface directions.

It is evident from fig. 2, it is evident that Si1 and Si2 components show XPD oscillations, while components Si3 and Si4 do not. The component Si1 was assigned to the Si involved in the c(2x2) structure. Conversely, the smaller Si2 , Si3 and Si4 components, resolved here in the higher binding energy side of the photoemission spectra, do not have a straight assignment. We have calculated the angular position of this maximum of interference for the surface atomic model of the Si-Cu(110) surface (upper part of fig. 1) alloy using a SSC formalism. The results of this calculation are indicated in fig. 2 by arrows. The angular position of the interference peaks for the components Si1 and Si2 is the same, indicating that the local atomic environment of the Si emitting atoms should be the similar. Therefore, the atomic structure of Si2 atoms should be the same of Si1. The Si3 and Si4 components do not present anisotropy for XPD azimuthal scans recorded at very grazing emission angles (72°). This could indicate a lack of local order and/or that the emitting atom is not placed on the surface.

FIGURE 2

XPD azimuthal scans around the [001] surface direction at 295 eV of kinetic energy of the different components of the spectra of figure 1. Polar angle set at 72°. The arrows indicate the position of the first order of interference inferred from a SSC calculation for the surface alloy model.

Taking into account the morphological description of the surface obtained by the STM, the different components of the XPS peak can be assigned to the different topographic features. The main Si2p peak Si1, is unambiguously assigned to the c(2x2) terraces, and its atomic arrangement corresponds to the c(2x2) structure observed in the inset of fig. 1. As discussed previously the local atomic environment of the Si atoms associated to the Si2 component of the XPS Si2p core level should be the same as for Si1, i.e. the corresponding Si atoms should also form a c(2x2) superstructure. Therefore, the Si2 component can be assigned to the Si alloy present in some islands visible on the surface with the STM. However, there is also surface alloy underneath these islands. These buried Si atoms present a different atomic environment and so they will contribute to the photoemission spectrum as a shifted peak. The fact that these atoms are embedded in the second layer would be reflected in the XPD spectra as absence of anisotropy for high emission angles. Therefore, the buried Si atoms underneath the islands can be assigned to the Si3 component of the XPS spectrum. The atomic assignment of the component Si4 is also clear. Si4 does not show photoelectron diffraction anisotropy in the azimuthal scans of fig.2. Moreover, this component increases importantly with coverage (data not shown) dominating the Si 2p XPS spectrum for a coverage higher than 2 ML, while the Si1-Si3 components result attenuated keeping, furthermore, constant their relative spectral intensity ratios. All these findings suggest that Si4 is associated to some Si clusters present on the surface.

REFERENCES (1).-J.A. Martín-Gago, R.Fasel, J. Hayoz, R.G. Agostino, D. Naumovic', P.Aebi and L. Schlapbach, Phys. Rev B.55, 12896(1997).
(2).- C. Rojas, C. Polop, J.A. Martín-Gago, E. Román, R. Gunnela, B. Brena, D. Cocco and G. Paolucci. Phys. Rev. B 57, 4493-4499 (1998)
(3).- C. Polop, C. Rojas, E. Román, J.A. Martín-Gago, B. Brena, D. Cocco and G. Paolucci. Surf. Sci. 407,268-274(1998)
(4).- J.A. Martín-Gago, C. Rojas, C. Polop, J.L. Sacedón, E. Román and G. Paolucci, Phys. Rev. B,59(1999)3070

GROWTH OF ULTRATHIN Fe FILMS ON $Cu_3Au(001)$

authors

F.Bruno
L.Floreano
R.Gotter
C.Mannori
A.Verdini
(Laboratorio TASC-INFM, Trieste, Italy)
M. Canepa
R. Moroni
S.Prandi
R.Mattera
S. Terreni
(University of Genova, Italy)
D.Cvetko
(Sincrotrone Trieste, Italy)

The magnetic properties of crystals are strongly affected by their microscopical structure. For the particular case of Fe, a few theoretical models predict it to display both ferromagnetic and antiferromagnetic phases, depending on the volume of the unit cell. A proper choice of the substrate allows the growth of thin Fe overlayers with structures different from the bcc bulk one. The $Cu_3Au(001)$ substrate has a lattice parameter (3.75 Å) which lies closer to the ferromagnetic fcc iron phase (3.66 Å) than to the ferromagnetic bcc iron (4.07 Å). Despite several experimental studies, the behaviour of this system is still not completely understood: with increasing thicknesses, the film exibits a spin reorientation transition from perpendicular to in-plane(1) and a structural transition from fcc to bcc(2), but there is no agreement neither on the transitions critical thicknesses, nor on the correlation between the two phenomena.

X-ray specular reflectivity, in-plane X-ray diffraction (XRD) and photoelectron diffraction (PED) have been employed in a structural study of the Fe/$Cu_3Au(001)$ system on the ALOISA beamline.

First the substrate surface has been structurally characterized at room temperature (RT), then iron has been deposited with different film thicknesses at RT.

X-ray reflectivity as a function of the photon energy between 3 and 8 keV has been measured before and after the deposition of the thicker film (18 Å). This technique allows to determine the average film thickness with an accuracy of 0.05 Å, hence calibrating the deposition flux. An estimate of the roughness of the interfaces can also be extracted, showing that the film interfaces are not significantly rougher than the clean substrate surface.

The structural characterization of each Fe film has been obtained via XRD and PED. In particular in-plane XRD has been used to determine the lateral spacings of the film

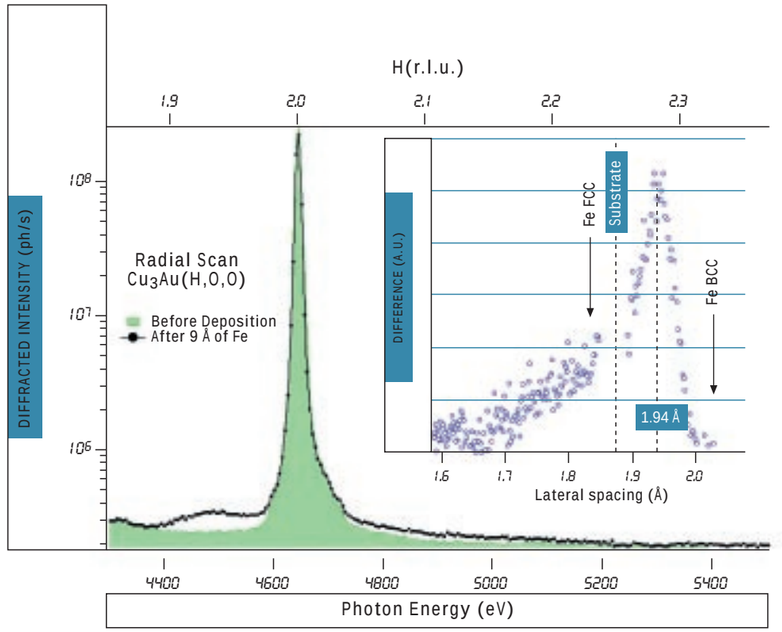

FIGURE 1

$Cu_3Au(H,0,0)$ radial scan obtained by varying the incoming photon energy at fixed grazing angle. The diffracted intensity before (shaded curve) and after the RT deposition of 9 Å (6 ML) of Fe (filled circles) is shown. In the inset the difference between the two scans exhibits a well defined peak which can be related to a lateral lattice spacing of 1.94 ± 0.01 Å. The corresponding half lattice parameters of the fcc substrate and Fe bcc bulk are indicated by the vertical arrows.

lattice by energy scans in correspondence of the (200) $Cu_3Au(001)$ diffraction peak, i.e. (H,0,0) radial scans in the reciprocal lattice. PED has been employed in forward scattering conditions to determine the corresponding vertical spacing of the topmost layers; both $Fe_{L,M,M}$ Auger (kinetic energy 642 eV) and Au 4f photoemission peaks (kinetic energy 777 eV) have been used to take polar scans along the [100] and [110] directions while keeping the surface at fixed grazing angle, usually set below the critical value for total reflection in order to enhance the signal from the Fe overlayer.

For the “thick” film (18 Å), the XRD (H,0,0) radial scan around the (200) reciprocal lattice vector of $Cu_3Au(001)$ exhibits a clear peak for a momentum transfer corresponding to an interplanar distance of 2.03 ± 0.01 Å, precisely matching the Fe bcc (110) value. The bcc domains are hence rotated by 45° with respect to the substrate, and their average lateral size can be estimated from the rocking curve width to be 120 Å. For an interme-

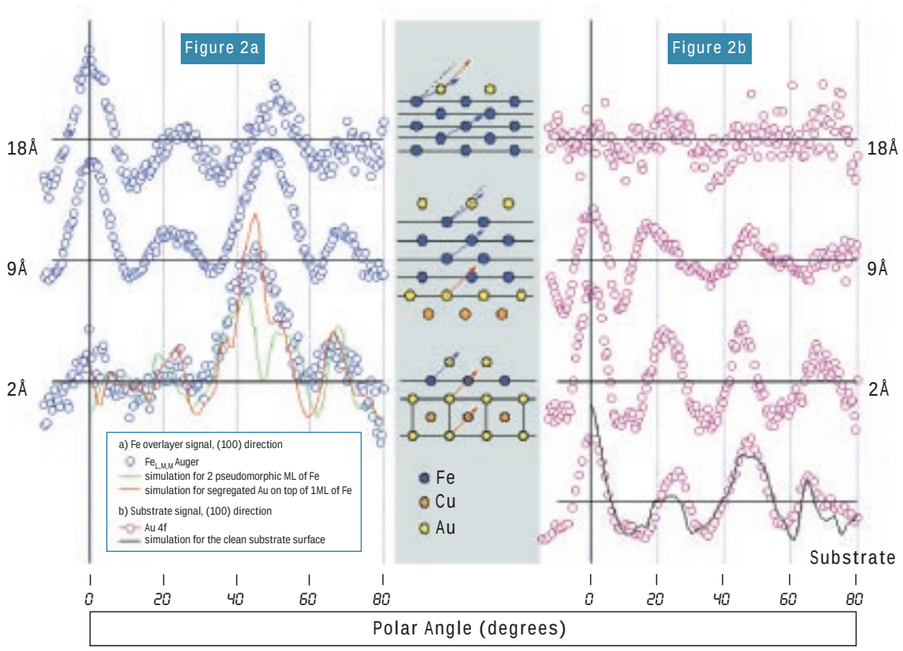

diate film thickness (9 Å) the measured spacing (half lateral lattice constant) is 1.94 ± 0.01 Å, i.e. approximately halfway between the Fe bcc (2.03 Å) and the fcc Cu_3Au(001) (1.87 Å) ones (Fig. 1). This result fully agrees with a very recent dynamical LEED analysis(3). In this case the domain size is reduced to 60 Å only. For a "thin" film of approximately 2 Å, it has not been possible to distinguish any diffracted beam separated from the substrate signal, thus suggesting that the lateral film spacing perfectly matches the substrate at the lowest thicknesses. We can take advantage of these results in the discussion of the PED measurements. Here we focus on the Fe and Au signals along the [100] direction (Fig. 2), starting now from the 2 Å film: a large peak at 45° from the sample normal dominates the polar scan on the Fe Auger signal, being shifted towards larger polar angles in the thicker films (Fig. 2a). Taking into account that Au surface segregation is expected to occur when depositing Fe at RT(4),we identify this feature with the strong focusing of the Fe emission by Au atoms segregated on top of the film and sitting in the fourfold absorption site, rather than the effect of Fe chains. This interpretation is supported by the simulations reported in Fig. 2a, from which the scattering element can be identified by the shape of the focusing peak. From the combination of XRD and PED, we can conclude that in the 1-2 ML range the Fe growth is pseudomorphic to the substrate. In the thicker films the Fe-Au bond angle moves away from the surface normal, as a consequence of the lateral expansion of the Fe topmost layers.

The determination of the Fe-Fe interlayer spacing requires accurate simulations of the polar scan along both directions, which are presently under way. Additional information might be extracted from the polar scans on the Au signal, which are reported for the [100] direction in Fig. 2b: the clean substrate anisotropy, together with the corresponding simulation, is shown for comparison. At 2 Å the amplitude of all the oscillating features is significantly increased, thus confirming the pseudomorphic growth at this stage. At 9 Å the Au anisotropy is damped at high polar angles, while at 18 Å the signal is almost featureless, probably originating from the segregated atoms(5).

FIGURE 2

a) Polar anisotropy of the $Fe_{L,M,M}$ Auger transition line (kinetic energy 642 eV) taken along the [100] direction of the Cu_3Au(001) for three typical thicknesses. At 2 Å the strong feature at 45° is reproduced much better by the simulated Fe-Au forward scattering than by the Fe-Fe focusing peak shape. The Fe-Au focusing shifts to higher polar angles with increasing thickness.
b) Polar anisotropy of the corresponding Au 4f emission. The signal from the clean substrate is reported for comparison, together with the simulated signal. At increasing Fe overlayer thickness, the anisotropy is first enhanced and successively damped; at 18 Å the Au yield is basicly isotropic, probably originating from the atoms segregated at the Fe-vacuum interface.

REFERENCES (1) F. Baudelet, M. - T. Lin, W. Kuch, K. Mainel, B. Choi, C. M. Schneider, J. Kirschner, Phys. Rev. B 51, 12563 (1995)
(2) M .- T .Lin, J. Shen, W. Kuch, H. Jenniches, M. Klaua C. M. Schneider, J. Kirschner, Surf. Sci. 410, 290 (1998)
(3) B. Schirmer, B. Feldmann, M. Wuttig, Phys. Rev. B 58, 4984 (1998).
(4) R. Opitz, S. Löbus, A. Thissen, R. Courths, Surf. Sci. 370, 293 (1996); B. Feldmann, B. Schirmer, A. Sokoll, M. Wuttig, Phys. Rev. B 57, 1014 (1998)
(5) F. Bruno, L. Floreano, R. Gotter, C. Mannori, A. Verdini, M. Canepa, R. Moroni, S. Prandi, R. Mattera, S. Terreni and D. Cvetko, Appl. Surf. Sci. (in press).

AU INDUCED GIANT FACETING OF VICINAL SI(001)

Adsorbate induced faceting and control of step arrangement on vicinal single crystal semiconductor surfaces are key techniques in the self-organized formation of 1-dimensional mesoscopic structures. Utilizing selective deposition techniques growth of nano wires will be possible by decoration. Crucial for the success of this kind of surface manipulation are the control of key parameters such as the width, length and height of ordered step bunches, the straightness of the step edges, and the regularity of the arrangement of atomic steps or step bunches.

a u t h o r s

F.-J. Meyer zu Heringdorf
R. Hild
P. Zahl
M. Horn-von Hoegen
(Institut für Festkörperphysik, Universität Hannover, Germany)
Th. Schmidt
S. Heun
B. Ressel
(Sincrotrone Trieste, Italy)
E. Bauer
(Arizona State University, Dept. of Physics & Astronomy, Tempe, USA)

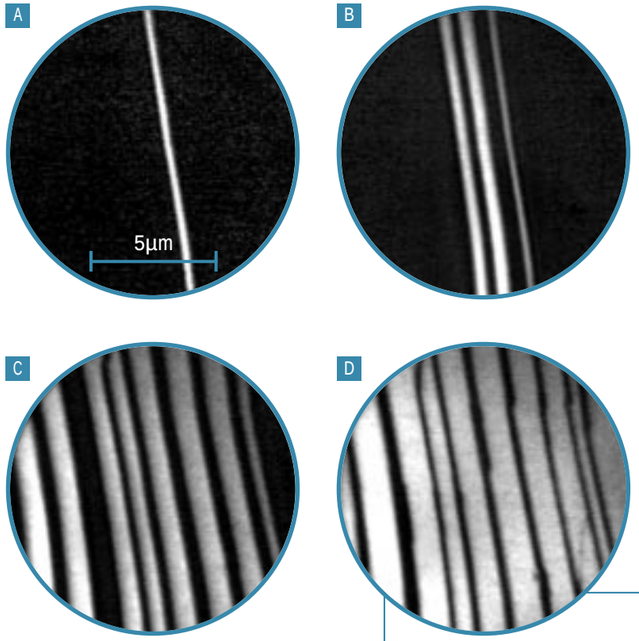

FIGURE 1

Sequence of 4 LEEM images which show the formation of elongated (001) terraces in-situ during Au adsorption at 860 °C. Bright field image conditions. Field of view is 12 µm. 7eV electron energy.

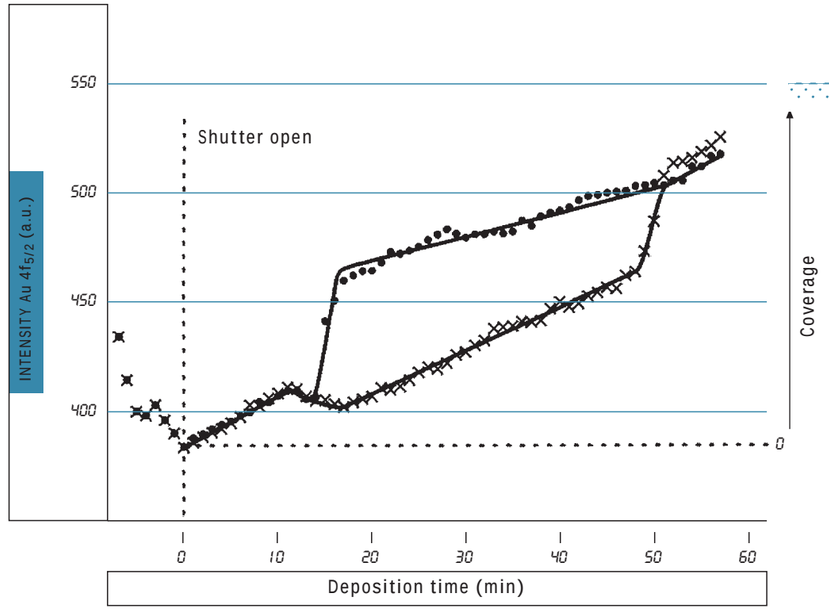

FIGURE 2

Normalized intensity of the Au $4f_{5/2}$ photo electron peak from an elongated (001) terrace (dots) and from an area with step-bunches/facets (x-marks). Photon energy was 128.5 eV. At ~14 min deposition time an elongated terrace nucleates which results in a separation of the local Au coverage.

Metal induced faceting of 4° vicinal Si(100) has excellent potential for this technique of self-organized formation of nano wires: the substrate shows perfectly ordered terraces with a width of 4 nm separated by double steps. Adsorption of Au at 800°C results in a dramatic change of the step morphology. The surface decomposes into areas which are perfectly flat with a (001)-orientation and (119)-facets, which compensate the macroscopic miscut. Extremely straight super terraces with a length limited only by the size of the sample (here 4 mm) and an average width of 1000 nm are formed by extensive Si mass transport. The extreme aspect ratio of 1:10000 of these sub-micron structures is explained by a heterogeneous nucleation process.

The kinetics of the faceting process have been studied during Au adsorption at 800°C with the spectroscopic photoemission and low energy electron microscope (SPELEEM) at Elettra. Single images are shown in Fig.1. The bright objects are the elongated (001) terraces which crystallize with a speed of propagation of up to 100µm/s. The steps of the initial surface are accumulated in irregu-

lar step bunches. With increasing Au coverage the step bunches are transformed into well defined facets with (119) orientation, as determined by SPA-LEED.

The driving force for the surface phase separation is the increasing Au coverage and the formation of an Au induced "(5 x 3.2)" reconstruction on the (001) terraces. Such a 2-dimensional crystallisation process has been studied for the first time with spatially resolved photoelectron spectroscopy using the energy analyser of the SPELEEM. The morphological phase separation is accompanied by a phase separation of the local Au coverage.

Fig. 2 shows that the Au coverage increases linearly up to a critical coverage of 1/3 of a monolayer where the first (001) terrace is nucleated. Then the local Au coverage increases drastically on the (001) terraces at the expense of the Au coverage on the irregular step bunches. This shows that first a critical (stable) nucleus must be formed, which has a higher Au coverage than the step bunches. This nucleus grows with a propagating crystallization front by collecting Au from the surrounding areas which results in a phase separation both in structure and the Au coverage.

STRUCTURE OF THE VIRULENCE FACTOR OF A PATHOGENIC BACTERIUM: THE MACROPHAGE INFECTIVITY POTENTIATOR PROTEIN FROM *LEGIONELLA PNEUMOPHILA*

authors

Alan Riboldi-Tunnicliffe
Rolf Hilgenfeld
(Institute of Molecular Biotechnology, Jena, Germany)
Franco Zanini
Adolfo Savoia
(Sincrotrone Trieste, Italy)

Legionella pneumophila is the causative agent of Legionnaire's disease, a severe pneumonia which in 1975 spread among participants of a convention of the American foreign legion in Philadelphia. The pathogenic bacterium can be found in showers, jacuzzis, and water pipes, and is harmful to people with impaired immune defense. The current outbreak of the disease in The Netherlands, with more than 200 people infected, of whom more than 20 have died, is a manifestation of the virulence of this pathogen.

FIGURE 1

There are two zinc atoms found between symmetry related C-terminal domains. Both zinc atoms are tetrahedrally coordinated. Zinc one is coordinated by GLU 164 from one molecule and HIS 205 from the second molecule, and two waters. Zinc two is coordinated by GLU 130 and 3 water molecules.

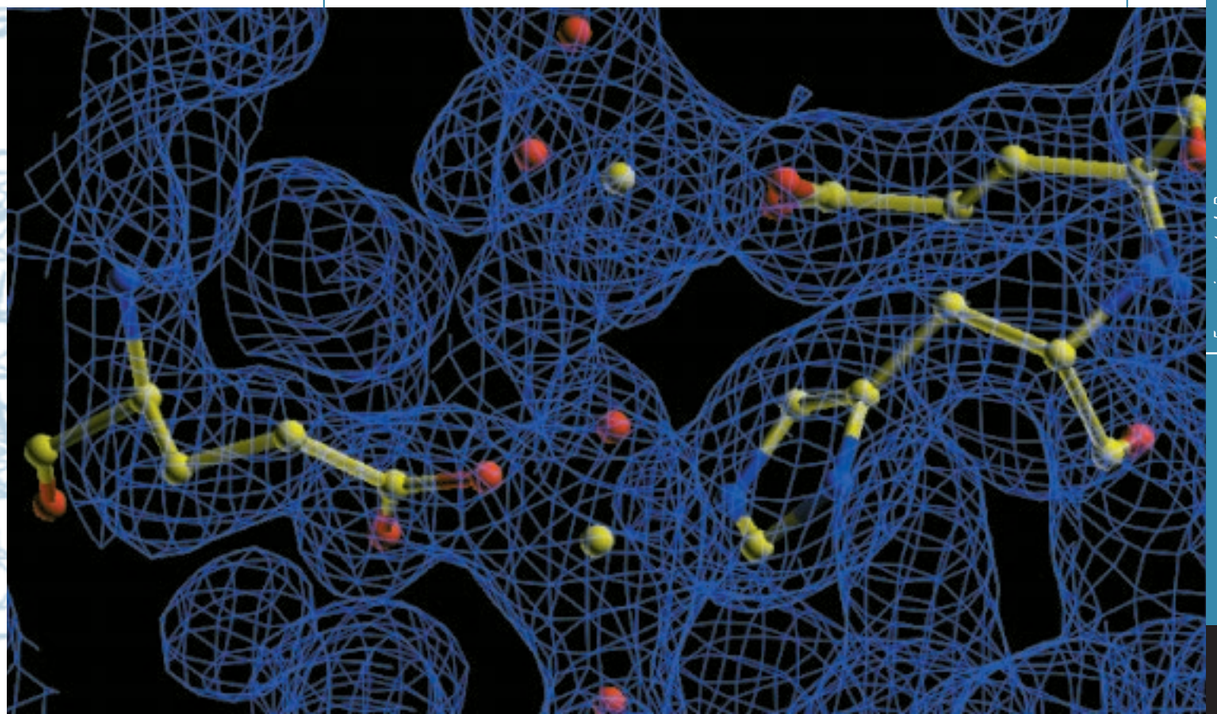

The major virulence factor of *Legionella pneumophila* is the Macrophage Infectivity Potentiator (Mip) protein. It is required for an efficient survival of the pathogen as an intracellular parasite in human macrophages. Similar Mip proteins are also found in *Chlamydia* (now believed to be involved in arteriosclerosis) and in trypanosomes, as well as in *Salmonella typhimurium*. Most interestingly, Mip proteins contain a C-terminal domain (107 amino acid residues) that displays peptidyl-prolyl *cis/trans* isomerase (PPIase) activity, *i.e.* it catalyzes the *cis/trans* conversion of peptide bonds preceeding proline residues in proteins. This enzymatic activity, the biological purpose of which is unknown, can be inhibited by the immunosuppressive drugs FK506 and rapamycin. Using multiwavelength anomalous dispersion (MAD) of zinc-containing Mip crystals at Elettra, we determined the three-dimensional structure of *Legionella* Mip in order to provide a basis for structure-based drug design.

Experimental

The protein has a molecular weight of 24 kDa and was expressed in the recombinant *E.coli* strain HB101. Crystals were grown at 288 K using the hanging drop vapour diffusion method. They grew to a maximum size of 0.3 x 0.3 x 0.3 mm in 10 days and belonged to the tetragonal spacegroup $P4_32_12$ with unit cell dimensions of a=b=80.7, c=103.4 Å and one molecule per asymmetric unit. High concentrations of zinc acetate proved necessary to obtain the crystals, even though zinc was not known to bind to the protein. Since the conventional isomorphous replacement approach was not successful, we decided to perform a MAD experiment. A fluorescence spectrum was recorded around the Zn edge, directly from the frozen crystal, to determine the point of inflection. The experiment was carried out at the following 3 wavelengths: 1.282, 1.295 and 1.268Å. The crystal diffracted to beyond 2.4 Å.

Two zinc ions were located by direct methods. They are responsible for a substantial portion of the crystal contacts. Their positions were refined using SHARP and the phases further improved using solvent flipping as implemented in SOLOMON. This resulted in a readily interpretable map (Fig. 1). The structure was refined to 2.4 Å resolution (R_{free} = 25 %).

Mip protein turned out to have a most unusual dimeric structure (Fig. 2). It shows a novel N-terminal dimerisation domain consisting of six helices (three helices from each monomer). The C-terminal domain is a typical FK506-binding domain with 5 ß-sheets and a small helix. The two domains are linked by a very long alpha helix, which is free standing and not involved in crystal contacts. Drug design efforts using this target structure are now being initiated.

FIGURE 2

The biologicaly active form of MIP is a dimer which is shown in the ribbon plot above. Also shown are the two zinc atoms and their coordinating waters.

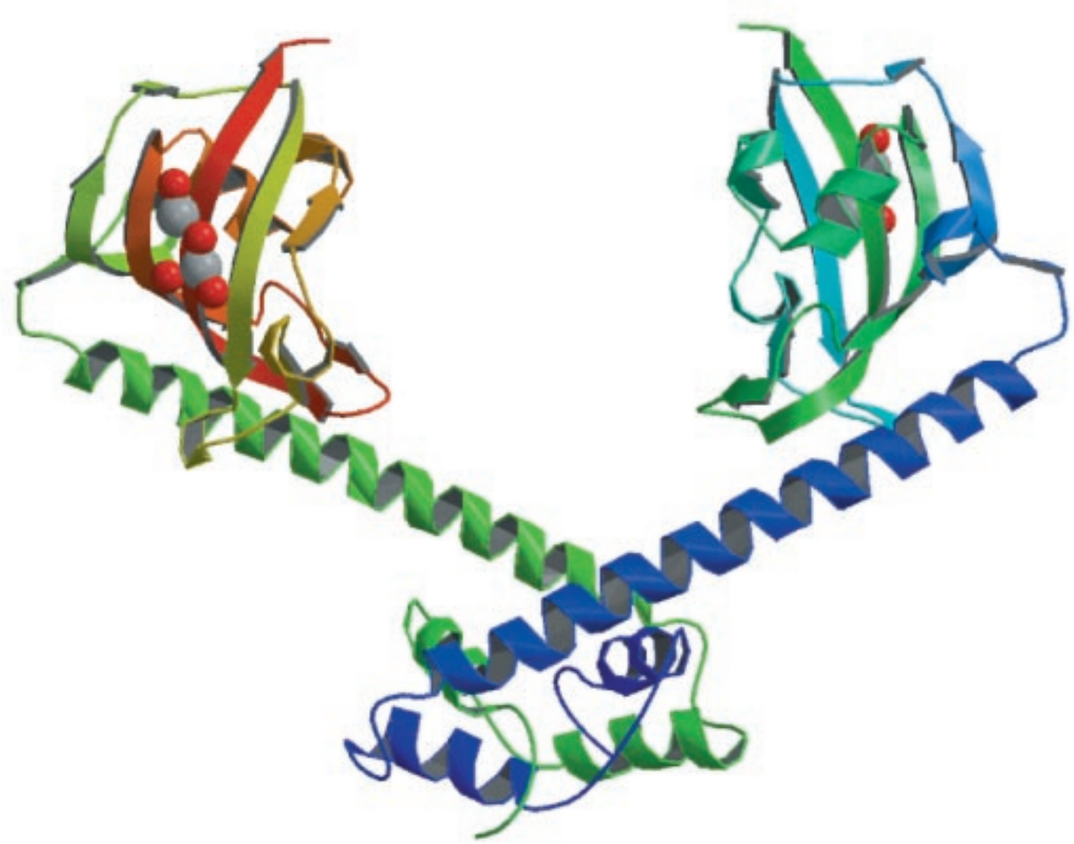

"BACK DOOR" OPENING IMPLIED BY THE CRYSTAL STRUCTURE OF A CARBAMOYLATED ACETYLCHOLINESTERASE

authors

C. Bartolucci
E. Perola
L. Cellai
(Istituto di Strutturistica Chimica "G. Giacomello", CNR, Roma, Italy)
M. Brufani
(Dipartimento di Scienze Biochimiche "A. Rossi-Fanelli", Università degli Studi di Roma "La Sapienza", Italy)
D. Lamba
(Istituto di Strutturistica Chimica "G. Giacomello", CNR, Sezione di Trieste, Italy)
(International Centre for Genetic Engineering and Biotechnology, Trieste, Italy)

Acetylcholinesterase (AChE) plays a fundamental role in the regulation of impulse transmission, terminating the action of the neurotransmitter acetylcholine. AChE inhibitors are widely employed in the symptomatic treatment of diseases involving acetylcholine depletion, like Alzheimer's disease (AD), glaucoma and myastenia gravis. AChE is one of the most efficient enzymes studied so far, and its catalytic mechanism, although thoroughly studied, is still the object of deep investigation.

The crystal structure of AChE from *Torpedo californica* revealed that the active site, constituted by a catalytic triad and a so-called anionic sub-site, is located at the bottom of a deep and narrow gorge. The anionic sub-site recognises the quaternary ammonium group of the substrate, while the catalytic triad, formed by Glu327, His440 and Ser200, is responsible for its resultant hydrolysis. At the entrance of the gorge, there is a regulatory site called the "peripheral anionic site". There is structural evidence that residues Trp84 and Trp279 play a central role in the catalytic and peripheral anionic sites, respectively. The presence of a strong electrostatic dipole directed towards the bottom of the gorge has been pointed out. Such a dipole should be unfavourable to the clearance of the cationic product choline, in apparent contrast with the high catalytic rate of the enzyme. The presence of a "back door" at the bottom of the catalytic pocket has been hypothesised, and its actual existence is still the object of a great controversy.

The first and thus far the only, two drugs, Cognex@ and Aricept@, approved by the United States Food and Drug

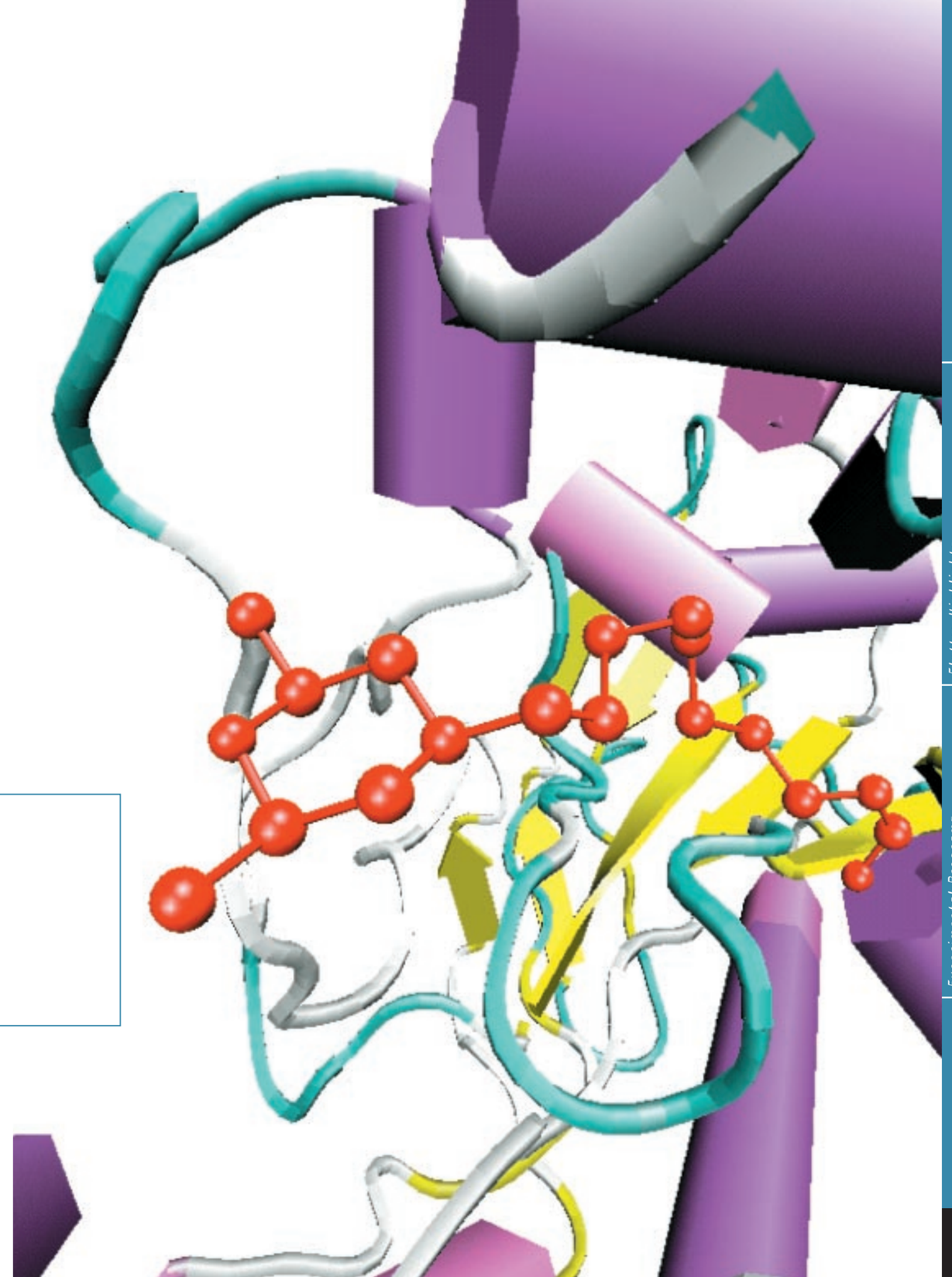

FIGURE 1

Schematic drawings of physostigmine, heptastigmine and MF268.

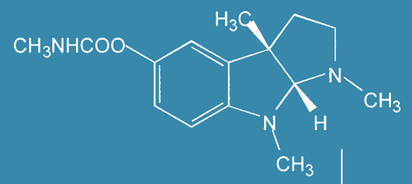

Physostigmine

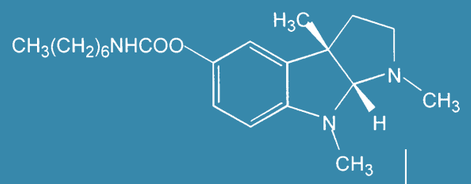

Heptastigmine

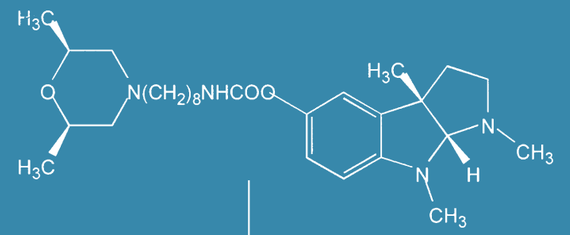

MF268

Administration for the treatment of AD are both reversible inhibitors of AChE. There is still a lack of structural evidence of the complexes between AChE and its pseudo-irreversible and irreversible inhibitors. Among these, the analogues of physostigmine (ie. heptastigmine, see Scheme 1), have been widely studied as potential drugs for AD. These compounds belong to a large class of carbamate-like AChE inhibitors, whose mechanism of action is characterised by a fast carbamoylation of the catalytic serine followed by a slow regeneration of the active enzyme. The structure of a stable carbamoylated enzyme would provide an analogue of the intermediate of acetylcholine hydrolysis. A more recent semisynthetic analogue, MF268, which carries a dimethylmorpholino group at the end of the alkyl chain, forms an even more stable adduct with AChE, behaving *in vitro* as a practically irreversible inhibitor. Such stability led us to choose the complex AChE/MF268 as the ideal candidate for the planned structural studies.

We determined the 2.7Å resolution crystal structure of this complex [Bartolucci et al., *Biochemistry* (1999), 38, 5714-5719], which represents the first direct evidence of a carbamoylated AChE, a species which is known to form in the mechanism of action of all carbamate-like inhibitors. In the X-ray structure, the dimethylmorpholinooctylcarbamic moiety of MF268 is covalently bound to the catalytic serine. The alkyl chain of the inhibitor fills the upper part of the gorge, blocking the entrance of the active site (see Fig. 1). This prevent eseroline, the leaving group of the carbamoylation process, from exiting through this path. This represents an indirect evidence that a "back door" opening may occur and shows that the release of products via a "back door" is a likely alternative for this enzyme.

The present crystal structure determination of the AChE/MF268 complex sheds light on two important questions widely debated so far:

i) the location of the leaving group after the carbamoylation step, with implications concerning the actual existence of a "back door" in the catalytic pocket, and

ii) the reasons for the great stability to hydrolysis of long chain carbamoylated adducts of AChE.

We are currently studying the details of the molecular recognition events that determine this mechanism. We also attempt to explain the differential specificity of MF268 for AChE and butyrylcholinesterase. This information should be of value for the design and analysis of analogues of physostigmine with improved affinity and selectivity.

FIGURE 2

The AChE/MF268 complex. Ribbons diagram showing the complex of the drug bound to the enzyme.

NON-EQUILIBRIUM RESPONSE-KINETICS OF PHOSPHOLIPID BILAYERS IN THE BIOLOGICALLY RELEVANT Lα-PHASE

authors

G. Pabst
M. Rappolt
H. Amenitsch
P. Laggner
(Institute of Biophysics and X-ray Structure Research, Austrian Academy of Sciences, Graz, Austria)
S. Bernstorff
(Sincrotrone Trieste, Italy)

Phospholipids, the main constituents of the biological membrane-matrix, display a distinct polymorphism depending on thermodynamic parameters (T, p, c). One-dimensional bilayers, two-dimensional tubular or three dimensional networks are only a few examples for the structural variety of the supra-molecular associates, wherein the lamellar liquid crystalline phase (L_α) is the biologically most relevant phase.

Although much is known about the structures and properties of phospholipid phases under equilibrium conditions, little is understood about the kinetics and mechanisms of response processes in lipid bilayers under non-equilibrium circumstances, e.g. upon rapid changes one of the thermodynamic parameters. The high X-ray flux offered by third-generation synchrotron sources has generally enhanced the potential for carrying out real-time jump-relaxation studies [1-4]. Rapid temperature-jump (T-jump) experiments can be carried out using an infrared laser. The IR-laser apparatus successfully installed at the SAXS beamline [5] induces T-jumps in the order of 10 °C/ms. The structural changes of the phospholipid sample are recorded by time-resolved small-angle X-ray diffraction (time resolution: 5 ms). The lipid/water systems responds to the T-jump with a very fast discrete thinning of the parent membrane into a structural ordered liquid crystalline phase (L_{α^*}), within the first few milliseconds. The intermediate repeat distance then relaxes back into the equilibrium state lattice within a time-scale of seconds (Fig 1).

This type of response kinetics is well known and has been studied in detail before [3-7], but since no more than two orders of diffraction peaks were recorded the structure of the liquid crystalline intermediate remained

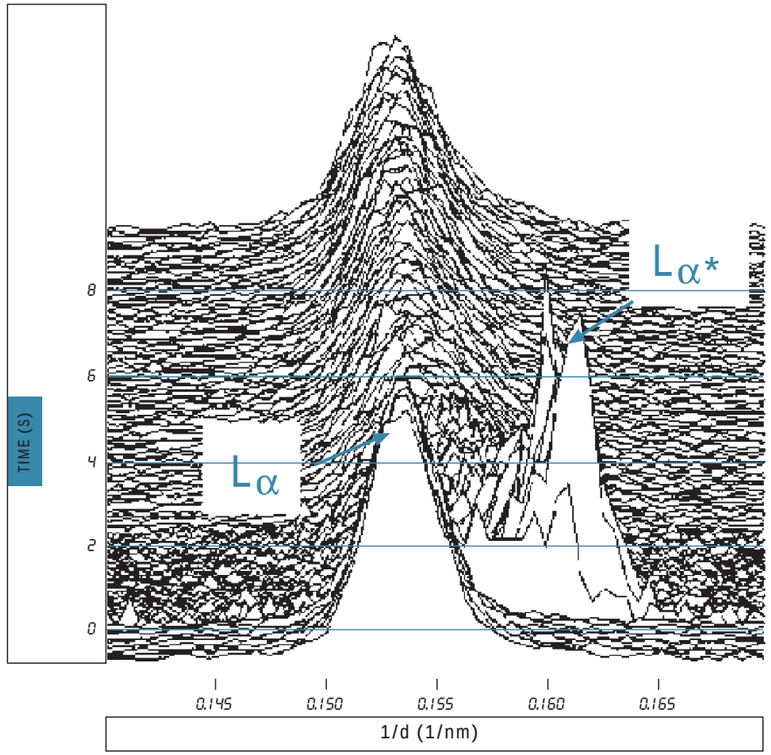

FIGURE 1

The first order diffraction peaks of a phospholipid sample during a T-jump experiment (time resolution = 5 ms). The IR-laser was triggered at time zero.

unknown. For the reliable calculation of an electron density distribution one needs at least four diffraction orders; the problem of missing higher orders is usually attributed to packing disorder. In a recent experimental session we made the effort to record four orders of Bragg peaks for a whole T-jump experiment for the system 1-stearoyl-2-oleoyl-*sn*-glycero-3-phosphoethanolamine (SOPE) / water. After determining the form-factors and the phases, the Fourier transform – yielding the electron density distribution – was calculated for the unit cell for each single time frame (Fig. 2).

The results show that the T-jump enforces a thinning of both the water layer as well as the bilayer itself, while the qualitative features of the electron density distribution remain the same. This suggests that the phospholipid membrane behaves like a spring that is pushed together and relaxes again to the equilibrium position after it is released ("mattress model"). This reveals on the other hand a highly cooperative interaction of the phospholipid molecules in the supra-molecular compound

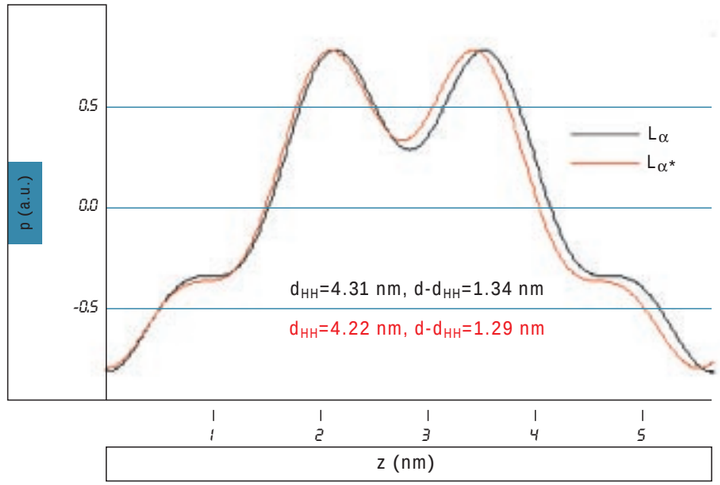

FIGURE 2

The effect of longitudinal multi-Superimposed electron density distributions of the original L_α-phase (black line) and of the intermediate phase L_{α^*} (red line) immediately after the laser flash.

of a membrane. For cell biology – where all processes like pore formation, self organization, switching processes, etc. are definitely non-equilibrium phenomena – the conservation of the membrane structure even under these extreme conditions is of high importance, since this is the only way of keeping up the vital function of the biological membrane in cell compartimentation and communication.

REFERENCES [1] M. Caffrey, G. Fanger, R.L. Magin and J. Zhang, Kinetics of the premelting (L_{β}-$P_{\beta'}$) and main transition (P_{β}-L_α) in hydrated dipalmitoylphosphatidylcholine, Biophys. J., *58: 667-686, 1990.*
[2] S. M. Gruner, Time-Resolved X-ray Diffraction of Biological Materials, Science *238: 305-312, 1987.*
[3] Rapp and R. Goody, Light as a Trigger for Time-Resolved Structural Experiments on Muscle, Lipids, p12 and Bacteriorhodopsin, J. Appl. Cryst. *24: 857-865, 1991.*
[4] M. Kriechbaum and P. Laggner, States of Phase Transitions in Biological Structures. In: "Progress in Surface Science" (ed. S. G. Davidson), 51(3): 233-261, 1996.
[5] G. Pabst, H. Amenitsch, S. Bernstorff, C. Krenn, M. Rappolt and P. Laggner, Infrared-Laser T-jumps with 10^4 K/sec at the SAXS beamline, ELETTRA Highlights, 1997 and ELETTRA News Number 21 ,1998.
[6] M. Rappolt. Zeitaufgelöste Röntgenbeugung zur Untersuchung von Phasenübergängen an Modellmembranen. PhD thesis, University of Hamburg, 1995.
[7] P. Laggner, H. Amensitsch, M. Kriechbaum, G. Pabst and M. Rappolt, Trapping of Short-Lived Intermediates in Phospholipid Phase Transitions: The L_{α^*}-Phase, Faraday Discussion *111: 31-40 (1998).*

10 MS TIME-RESOLVED X-RAY DIFFRACTION OF THE CORE LIPID TRANSITION OF HUMAN LOW DENSITY LIPOPROTEINS

authors

M.Pregetter
R.Prassl
H.Amenitsch
P.Laggner
(Institute of Biophysics
and X-ray Structure Research
Austrian Academy of Sciences,
Graz, Austria)

Low Density Lipoproteins (LDL) present an important part of the human blood. They are responsible for the transport of lipids, i.e. cholesterol or triglycerides in blood circulation. Failure to function can result in atherosclerosis, followed by myocardial infarct or stroke.
The structure of LDL can be described by a quasispherical core-shell model, in which the apolar constituents (esterified cholesterol and triglycerides) form a core of about 150 Å diameter, which is surrounded by amphiphilic lipids (phospholipids, unesterified cholesterol) as seen in fig. 1. Depending on the blood donor, the protein LDL undergoes a major structural transition of the apolar core from the core liquid crystalline to the core isotropic state just below physiological body temperature, at about 25 to 32°C (T_m). In the outer extremities (finger tips, toes) the blood

FIGURE 1

Sketch of the LDL lipoprotein in the 3 different states: Temperature T < melting temperature T_m for ratio CE/TG < 7 and for ratio CE/TG > 7 (core liquid crystalline state), as well as for the $T > T_m$ (core isotropic state). TG, CE, FC, PL denotes triglycerides, esterified cholesterol, unesterified cholesterol, phospholipids.

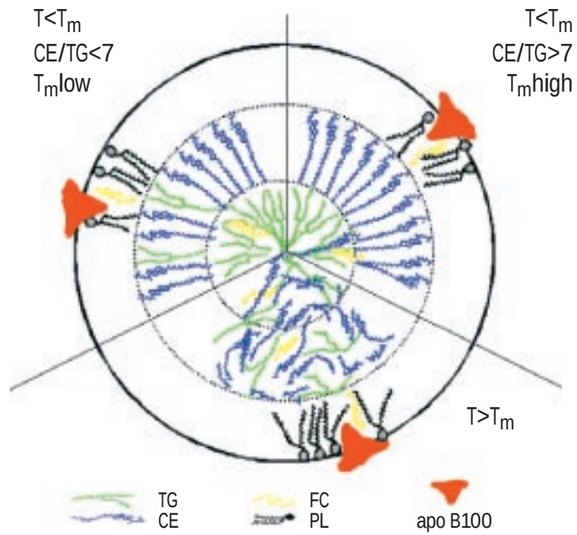

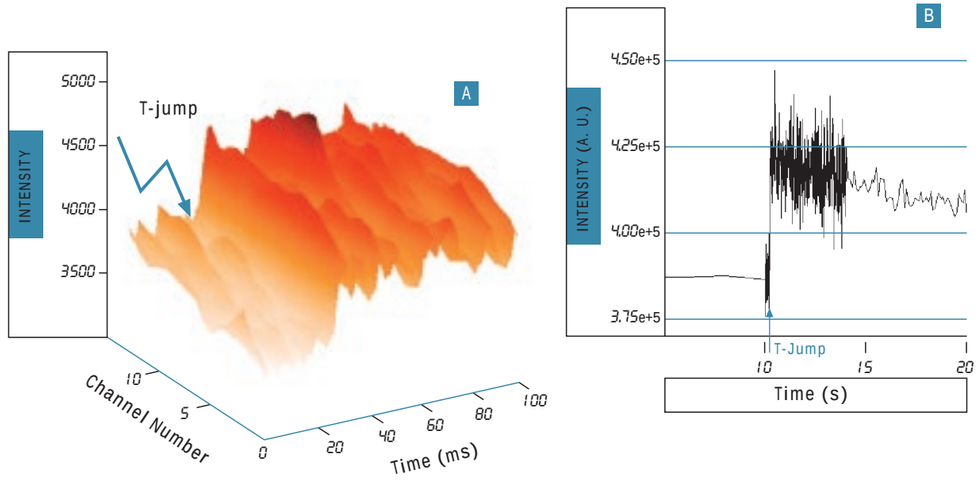

temperature allows for a transition of the LDL core towards its more rigid and radially ordered state.

Time-resolved measurements provide evidence on whether the kinetics of the structural transition permit the transition during the time LDL spends in cooler parts of the human body.

High precision SAXS curves in the range of $1.5.10^{-2} < h < 0.2$ Å^{-1} were measured on well defined subfractions of native LDL. An experimental set-up using an erbium-laser allowed temperature jumps from temperatures below to temperatures well above the core lipid transition an in extremely short time (fig.2). Following the temperature jump a series of measurements elucidated the kinetics of the core-transition. It can be stated that the transition from the rigid towards the fluid core of LDL takes place in less than the 10 ms time-resolution (fig.2). The rearrangement of the lipid core proceeded within one second.

FIGURE 2

A.) A sudden increase of the first side-maximum related to the core-melting is observed at the temperature jump.
B.) Integrated intensity of the first side maximum versus time. The transition to an isotropic state of the LDL core (core-melting) occurs faster than the 10 ms time-resolution.

REFERENCES [1] M.J. Chapman, P.M. Laplaud, G. Luc, P. Forgez, E. Bruckert, S. Goulinet and D. Lagrange (1988). J. Lipid Res. 29, 442-458.
[2] P. Laggner (1995) in Modern Aspects of Small-Angle Scattering (Brumberger H., ed) pp. 371-386, Kluver Academic Publishers, Leiden, Netherlands.
[3] R. Prassl, B. Schuster, P. Laggner, C. Flamant, F. Nigon and J.M. Chapman (1998). Biochemistry 37, 938-944.
[4] M. Kriechbaum, G. Rapp, J. Hendrix, P. Laggner (1989). Rev. Sci. Instrum. 60(7), 2541-2544.
[5] M.Pregetter, R.Prassl, B. Schuster,M. Kriechbaum, F. Nigon, J. Chapman, P. Laggner (1999). JBC 274(3)1334-1341.

PHASE CONTRAST AND DIFFRACTION ENHANCED MAMMOGRAPHY AT SYRMEP

authors

F. Arfelli
V. Bonvicini
G. Cantatore
E. Castelli
R. Longo
A. Olivo
S. Pani
P. Poropat
M. Prest
A. Rashevsky
L. Rigon
A. Vacchi
E. Vallazza
(Dipartimento di Fisica, Università di Trieste and INFN - Sez. di Trieste, Italy)
A. Bravin
R. H. Menk
G. Tromba
(Sincrotrone Trieste, Italy)
L. Dalla Palma
(Istituto di Radiologia dell'Università di Trieste, Ospedale di Cattinara, Trieste, Italy)

The high degree of coherence of third generation synchrotron sources such as Elettra offers the opportunity to investigate new X-ray imaging techniques that can be applied also to medical radiology [1-4]. In conventional radiography the image contrast is based on absorption effects expressed by the amplitude properties of X-rays detected by the image receptor. Taking advantage of the beam coherence, additional information can be obtained about the phase perturbations of the incident wave: both spatial and contrast resolution can be significantly enhanced. This progress becomes particularly important for the cases of weak absorbing samples where small differences in the absorption coefficients result in poor contrast images. In the field of medical radiology this is a characteristic case of mammography where the recognition of low contrast nodules and/or small calcifications inside a soft tissue matrix is needed to perform accurate breast cancer diagnosis.

Two novel imaging techniques have been implemented at the SYRMEP beamline to produce images of test objects and of *in vitro* tissue specimens enhanced by the coherence of the beam: PHase Contrast radiography (PHC) and analyzer crystal Diffraction Enhanced Imaging (DEI). For these studies images have been taken using standard medical screen-film systems [4,5].

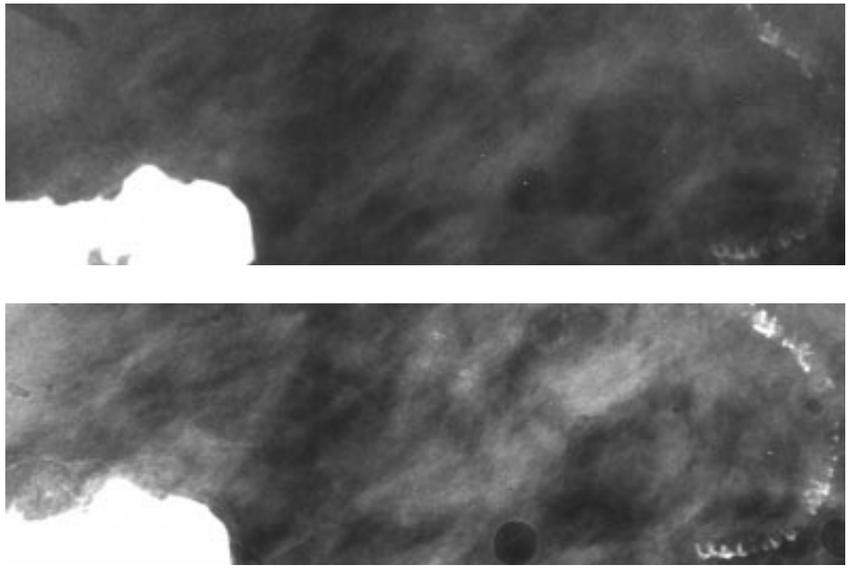

FIGURE 1

Images of a breast tissue specimen with patological calcifications obtained with the mammographic unit (A) and with the PHC technique (B).

In PHC radiography we are interested in the registration of the phase shifts produced on the incident wave by the sample and the details inside it. The interference pattern produced between the undiffracted and the diffracted (phase-shifted) wave occurs along the border of the objects inside a very narrow angular region. This signal can be detected if the distance between the sample and the detector matches with the detector spatial resolution. The implementation of this technique consists simply in selecting the sample-to-detector distance that maximize the interference signal and scanning the sample and the detector through the beam using two independent movement stages. The produced diffraction pattern appears superimposed to the conventional absorption image on the film.

In the DEI set-up, an analyzer Si(111) crystal, in addition to the channel-cut Si(111) crystal used as monochromator, is placed between the sample and the detector to select the angular emission of X-rays exiting the sample. This crystal is supplied with appropriate motion control to allow a fine tuning with respect to the beam. Two ionization chambers are used to find out the alignment of the analyzer with respect to the monochromator, the latter is also used to evaluate the film exposure.

The rocking curve of the two crystals is the same. Thus, when the analyzer is aligned with the monochromator (i.e. the (111) planes of the crystals are parallel), the former acts as a scattering rejecter: most of the photons scattered by the sample at angles larger than the FWHM of the analyzer rocking curve are rejected by the crystal.

If a slight misalignment between monochromator and analyzer is introduced, the reflectivity of the analyzer is maximized for X-rays deviated by a given scattering angle (equal to the misalignment angle). In this way it is possible to convert the photon diffraction angles, and thus phase shifts, into different reflectivity coefficients.

Since the scattering angle is – to first approximation – proportional to the gradient of the real part of the refractive index, the analyzer effectively converts the behavior of this real part of the sample into different reflectivity coefficients for the refracted wave, and consequently into intensity differences on the detector.

The effectiveness of these techniques can be evaluated by comparing the images of different tissue specimens and test objects obtained at the beamline and at a clinical mammographic unit with the same screen-film system devices [4,5].

A comparison between a conventional radiography and a PHC image of a human breast tissue specimen containing a calcification and some calcium deposits can be done by observing Fig.1a and 1b. The delivered mean glandular dose is the same (≈ 1.5 mGy) for the two images. In the PHC image (Fig. 1b) the visibility of the details is enhanced; furthermore, as opposed to the conventional image (Fig. 1a), one can observe that the calcification is

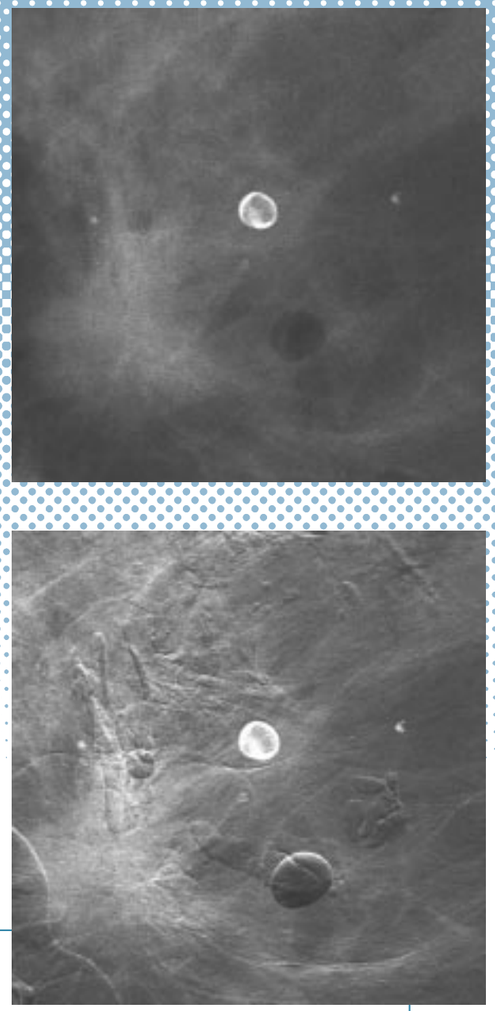

FIGURE 2

Images of a breast tissue specimen obtained with the mammographic unit (A) and with the DEI technique (B).

surrounded by soft tissue having varying thickness. The density of this tissue can be recognized from the opacity. In the right side of this image one can also clearly see an extended vascular calcification.

The images of another human breast tissue sample obtained at the mammographic unit and with the DEI technique at 17 keV are shown in Fig. 2a-2b. The conventional image (Fig. 2a) has been taken with a mean glandular dose of 0.8 mGy. In the DEI image, which was taken with a mean glandular dose of 0.6 mGy (Fig. 2b), the contrast as well as the resolution are enhanced. This results in an improved definition of the glandular component and of the visibility of calcifications.

Both the imaging techniques can allow significant improvements in mammography and do not require an increase in the delivered dose. Further investigations have to be carried out to complete the understanding of the DEI technique. Certainly these novel imaging techniques will have a great impact in the near future of medical applications when applied to *in-vivo* investigations.

REFERENCES [1] A.Snigirev, I.Snigireva, V.Kohn, S.Kuznetsov, I.Schelokov, Rev. Sci. Instrum. 66 (12), (1995), p. 5486-5492.

[2] D. Chapman, W.Thomlinson, R.E. Johnston, D.Washburn, E.Pisano, N.Gmur, Z.Zhong, R.Menk, F.Arfelli, D.Sayers, Phys. Med. Biol. 42 (1997), p.2015-2025.

[3] M.Di Michiel, A.Olivo, G.Tromba, F.Arfelli, M.Assante, V.Bonvicini, A.Bravin, G.Cantatore, E.Castelli, L.Dalla Palma, R.Longo, S.Pani, D.Pontoni, P.Poropat, M.Prest, A.Rashevsky, A.Vacchi, E.Vallazza, Proceedings of Haga Conference 1997, Springer-Verlag ed., p.78-82.

[4] F.Arfelli, M.Assante, V.Bonvicini, A.Bravin, G.Cantatore, E.Castelli, L.Dalla Palma, M.Di Michiel, R.Longo, A.Olivo, S.Pani, D.Pontoni, P.Poropat, M.Prest, A.Rashevsky, G.Tromba, A.Vacchi, E.Vallazza, F.Zanconati, Phys. Med. Biol, Vol.43, n.10, oct. 1998, p.2845-2852.

[5] F.Arfelli, V.Bonvicini, A.Bravin, G.Cantatore, E.Castelli, L.Dalla Palma, M.Di Michiel, M.Fabrizioli, R.Longo, R.H.Menk, A.Olivo, S.Pani, D.Pontoni, P.Poropat, M.Prest, A.Rashevsky, M.Ratti, L.Rigon, G.Tromba, A.Vacchi, E.Vallazza, F.Zanconati, Radiology (in press).

Technical Programs

AN EMBEDDED CONTROL AND ACQUISITION SYSTEM FOR MULTICHANNEL DETECTORS

authors

L. Gori
R. Tommasini
G. Cautero
D. Giuressi
M. Barnaba
A. Accardo*
S. Carrato*
G. Paolucci
(Sincrotrone Trieste, Italy)
*(D.E.E.I., University of Trieste, Italy)

A pulse counting multichannel data acquisition system, characterized by the high number of high speed acquisition channels, and by the modular, embedded system architecture was developed in the Beamline Special Instrumentation laboratory of Elettra [1]. The high number of high speed acquisition channels leads to very fast acquisitions and allows to obtain sequences of snapshots, for the study of time dependent phenomena. The the modular and embedded system architecture, thanks to the integration of a CPU into the system, provides high computational capabilities, so that the interfacing with the user computer, via a standard interface (IEEE 488) and/or by an Ethernet connection, is very simple and user friendly. Through these links, the user can specify the experiment parameters (number of channels, counting time window, energy range etc.). The embedded control system can also take control of the experiment by setting the polarising voltages of the electron analyser. In this way the system manages data acquisition autonomously and retains the acquired data until the user downloads them. Moreover, the user computer is free from control and acquisition tasks.

This system has been tested (fig.1) on a double pass hemispherical analyser [2] incorporating a multidetector of 96 discrete anodes which is going to be installed on the SuperESCA beamline, where it will be used for fast XPS experiments [3]. However, it must be kept in mind that its modular and embedded architecture allows it to be used in a large number of physics experiments, in those cases where position sensitive detectors are used. The analog part of the acquisition electronics is hosted in a box immediately outside the vacuum chamber, and consists of bias, coupling, and protection circuits, and of a preamplifier and thresholding unit. Each signal is suitably amplified by one channel of a 16 channel Microchannel Integrated Charge Amplifier (MICA) integrated circuit [4] which also converts the pulses into digital signals. This circuitry has been included in a set of hybrid circuits (CHYBA, Charge Hybrid Amplifier), each one processing 16 channels. The digital electronics section (i.e. counters and controls) has been implemented on PC/104 cards, thus obtaining a compact, lightweighted system. The counting section, consisting of 3 sets of 32 asynchronous 32 bit counters, has been built using several FPGA's, in order to reach the best compromise between performance, size, ease of upgrading, and cost. In particular, we used twelve pASIC2 2009 FPGAs by QuickLogic, which have been chosen because of their very high speed given by the 'antifuse' technology. Each counter has its own buffer, in order to implement a double buffered counting process. Consequently, after the end of a time window, pulse counting can be immediately started for the following time window while transferring the data of the previous one. This is of particular importance when the data acquisition time is comparable to the readout time. For 96 channels, for example, 384 bytes have to be transferred for each time

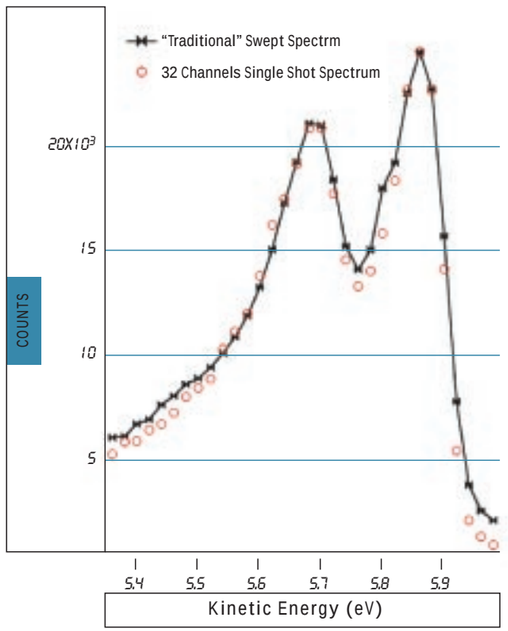

FIGURE 1

Spectrum of gas phase Argon $3p^{1/2}$ and $3p^{3/2}$ using as excitation source a UV lamp.

windows, which requires approximately 0.2 ms if a 2 MB/s channel bandwidth is available: this would be a 20 % overhead if using a 1 ms time window. Bench tests have shown a maximum count rate higher than $20*10^6$ counts/s The counters are connected to a controller FPGA by a simple proprietary Extensible Parallel Bus (EPB), which is used to control them and to address them during the reading phase. The EPB may be easily extended in order to communicate with other devices, by using several spare lines which already connect all the FPGA's. In fig. 1 we report the 96 channels snapshot spectrum of gas phase Argon $3p^{1/2}$ and $3p^{3/2}$ using as excitation source a UV acquired in less then 1 second and the "traditional" swept spectrum acquired in about 30 seconds; for both spectra the pass energy was 10 eV.

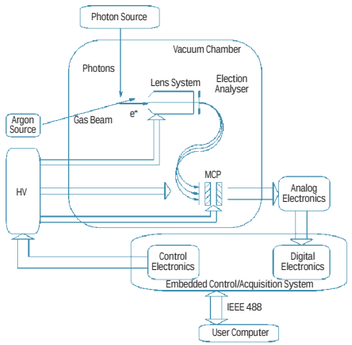

The Acquisition System

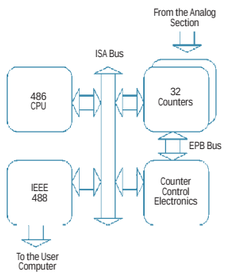

Digital Section

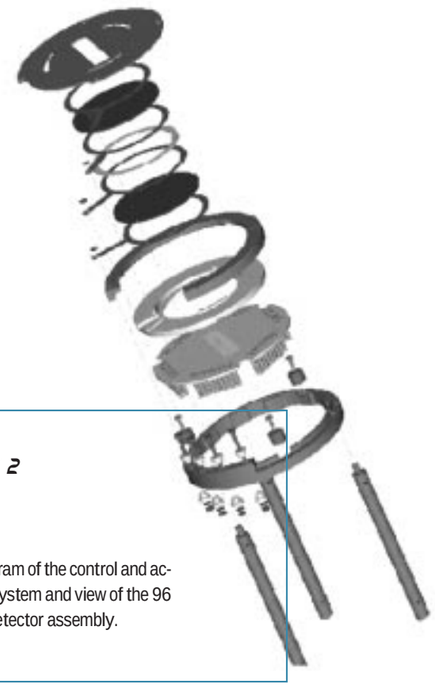

FIGURE 2

Block diagram of the control and acquisition system and view of the 96 channel detector assembly.

REFERENCES [1] L. Gori, R. Tommasini, G. Cautero, D. Giuressi, M. Barnaba, A. Accardo, S. Carrato and G. Paolucci, Nucl. Instr. Meth. Methods A431, 338 (1999).
[2] A. Baraldi and V. R. Dhanak, J. Electron Spectrosc. Relat. Phenom. 67(1), 211 (1994).
[3] A. Baraldi, M. Barnaba, B. Brena, D. Cocco, G. Comelli, S. Lizzit, G. Paolucci, R. Rosei, J. Electron Spectrosc. Relat. Phenom. 76, 145 (1995).
[4] C. C. Enz, F. Krummenacher, R. Bellazzini, Nucl. Instr. Meth. Methods A32, 543 (1993).

X-RAY WAVEGUIDES FROM THE MULTILAYER LABORATORY NOW PROVIDE A 5-FOLD GAIN IN AN X-RAY LINE FOCUS OF ONLY 140 nm

authors

S. Di Fonzo
W. Jark
G. Soullié

As in the visible range also hard X-ray photons can be confined bouncing back and forth in a thin film resonator as indicated in fig. 1. This will happen as long as the resonator has low absorption and the photons strike all interfaces below their respective critical angle for total reflection. Efficient traveling is only found when the incident wavefield excites a standing wave inside the resonator with the nodes at the interfaces. The latter situation is achieved only for discrete angles of incidence which depend on the photon wavelength and on the resonator thickness. The feeding mechanism is the evanescent wave in the cover layer, which couples intensity to the standing wave (for more detail see the extended reports [1-3]). The beam confinement leads to a compression of the incident beam in one direction. This has two interesting consequences: firstly a theoretical intensity enhancement even beyond 100-fold compared to the incident intensity is possible in the standing wavefield with perfect interfaces, and secondly at the termination of the waveguide the intensity is available in a very narrow line. Indeed we succeeded to produce in this way line-focii with only about 140 nm (0.14 microns) extend in one direction for 13 keV photons [3-4]. This is a beamsize, which has not been achieved yet by any other means in this energy range and it is well below the resolution of optical microscopes. If one considers the fundamental standing wave with an intensity maximum in the centre of the thin film and with its two nodes at the interfaces, the line focus should even have an extend of only half of the resonator thickness, in this case of 70 nm.

Real interfaces will not be perfectly smooth and thus one has to expect intensity losses in the wave travelling towards the waveguide termination. For simplicity the gain measured at the waveguide exit will be calculated as the ratio between the exiting intensity (homogeneously distributed over the resonator thickness) and the incident intensity, i.e. as the lower limit. With the recently measured gain of 5 we could pass rather significantly the break-even point for the first 3 resonance orders at a photon energy of 17 keV as is shown in fig. 2. Consequently the measured performance is significantly better than that obtainable with a simple slit, which may not be feasible with

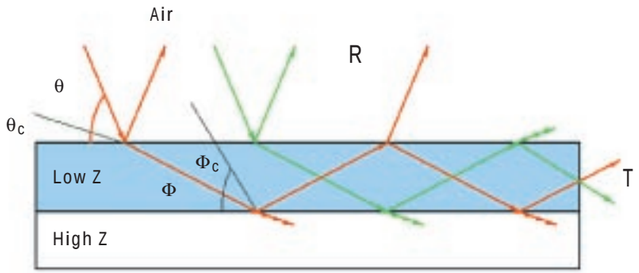

FIGURE 1

Cross-section of the X-ray waveguide used for this investigation.

0.14 micron opening, leaving still some margin for further improvements. The parameters affecting the system efficiency are: substrate flatness, the above mentioned interface roughness and the absorption in the resonator layer. Improvements in these parameters lead to the improvements of the waveguide efficiency by more than 2 orders of magnitude in the course of only 3 years.

The first prototype waveguides which we produced onto decently flat float glass substrates and measured at the beginning of 1995 at an unfocused undulator beam at BL1/ID13 at the ESRF (Grenoble, France) provided only about 0.003 - 0.03 gain in a 90 nm line [3].

Already at the end of 1995 with better beam coupler and resonator optimization we arrived almost at the break-even point [4]. And better interfacial roughness at flatter substrates provided slightly more than one year later (Febr. 1997) a gain exceeding 3 in a 0.14 micron line [5].

While the experiment at the first prototype could only be successfully concluded at a powerful ESRF undulator beamline, with the recent gain these objects can now also be used for less-demanding microspot experiments at sources with significantly smaller

FIGURE 2

Gain (ratio between incident beam intensity and intensity at the waveguide terminal) as measured for several travelling modes in an X-ray waveguide with resonator thickness 162 nm for 17 keV photon energy.

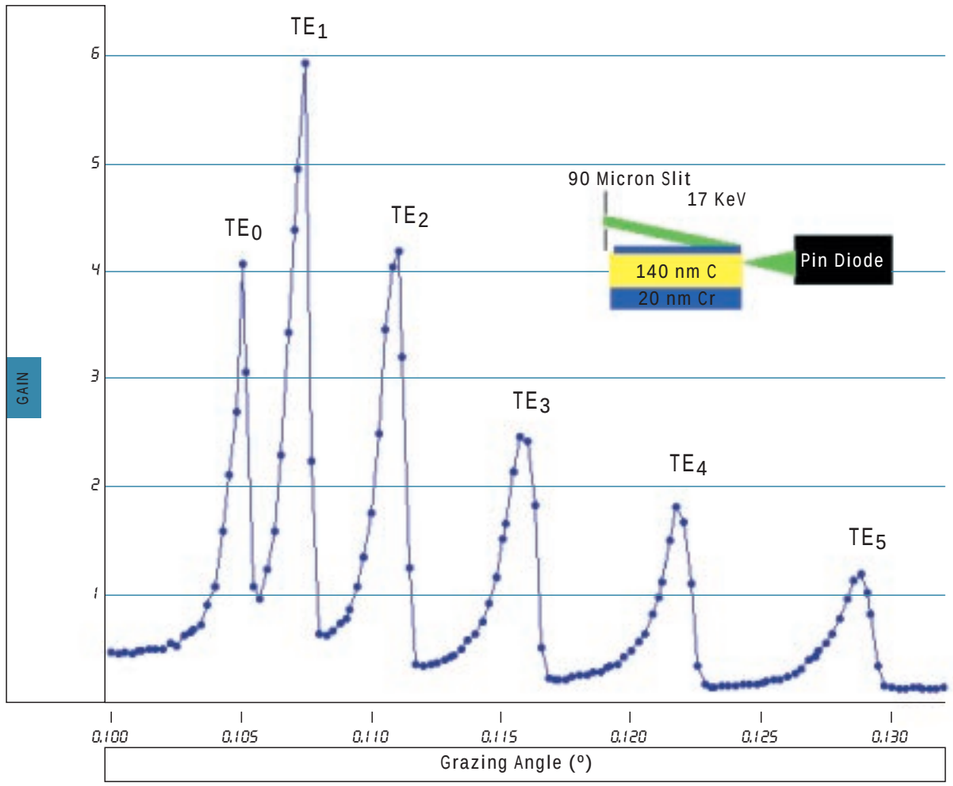

brightness. Indeed the newest result was obtained at BM5, which is the ESRF optics beamline installed at a bending magnet source. The potentiality of the divergent coherent beam exiting from the waveguide terminal for submicron X-ray phase constrast microscopy experiments could already be demonstrated impressively [5] and further related experiments are underway.

Some features of the waveguided beam are not readily achievable with focusing optics based on diffraction, however, they are highly appreciated by the experimenter:

- very low intensity in the intensity tails
- absence of overlapping higher order foci.

Indeed the beam confinement in the resonator will lead to diffraction at the waveguide termination in analogy to slit diffraction. As the electric field in the resonator is not constant but has nodes at the interfaces relatively less intensity is diffracted into secondary peaks. Consequently in the waveguide case only about 0.5% of the exiting intensity is diffracted into secondary peaks, i.e. into tails, while almost 10% of the intensity ends up in the tails in classical slit diffraction.

This project is a collaboration between the multilayer group of the SINCROTRONE TRIESTE (S. Di Fonzo, G. Soullié, W. Jark) and the Istituto di Elettronica dello Stato Solido of the CNR-Rome (S. Lagomarsino, A. Cedola and E. Di Fabrizio) and with the participation of several colleagues from the ESRF (C. Riekel of the Microfocus beamline (ID13), A. Freund and O. Hignette of the Optics beamline (BM5) and P. Cloetens of the topography beamline (ID19).

REFERENCES [1] E. Spiller and A. Segmüller, Appl. Phys. Lett. 24, 60 (1974)
[2] Y. P. Feng, S. K. Sinha, H.W. Deckman, J. B. Hastings and D. P. Siddons, Phys. Rev. Lett. 71, 537 (1993)
[3] S. Lagomarsino, W. Jark, S. Di Fonzo, A. Cedola, B. R. Müller, C. Riekel and P. Engstrom, J. Appl. Phys. 79, 4471 (1996)
[4] W. Jark, S. Di Fonzo, S. Lagomarsino, A. Cedola, E. Di Fabrizio, A. Brahm, and C. Riekel, J. Appl. Phys. 80, 4831 (1996)
[5] S. Lagomarsino, A. Cedola, P. Cloetens, S. Di Fonzo, W. Jark, G. Soullié and C. Riekel, Appl. Phys. Lett., 71, 18 (1997)

STATE-OF-THE-ART GASEOUS IMAGING DETECTORS FOR ADVANCED BIOLOGICAL DIFFRACTION STUDIES

authors

R. H. Menk
S.Bernstorff
(Sincrotrone Trieste, Italy)
A. Sarvestani
H. J. Besch
A. H. Walenta
(Fachbereich Physik,
Universität-GH Siegen, Germany)
H.Amenitsch
(IBR, Graz, Austria)

The public investment in modern synchrotrons has resulted in a tremendous development of both the sources as well as the associated X-ray optics. Unfortunately the development of the X-ray detection devices has not kept pace with that of the synchrotron light sources. Thus it is often the detector performance that limits the final data quality (e.g. Kriechbaum *et al.*, 1989; Helliwell *et al.*, 1993) and prevents the full exploitation of the facilities. This applies especially to applications such as time-resolved small angle X-ray scattering (SAXS) or protein crystallography, where the requirements in terms of detector performance are exceptionally high. In the following two novel systems are presented based on the principle of highly segmented gaseous detectors that represent a major step forward. Although gaseous detectors are often considered as “classical” or “old fashioned” devices, in combination with novel gas amplification structures such as the Micro-CAT (for a detailed description see Sarvestani *et al.*, 1998a) and sophisticated electronics they reveal unique features that make them a superior detection device and thus well suited for installation at modern beam lines.

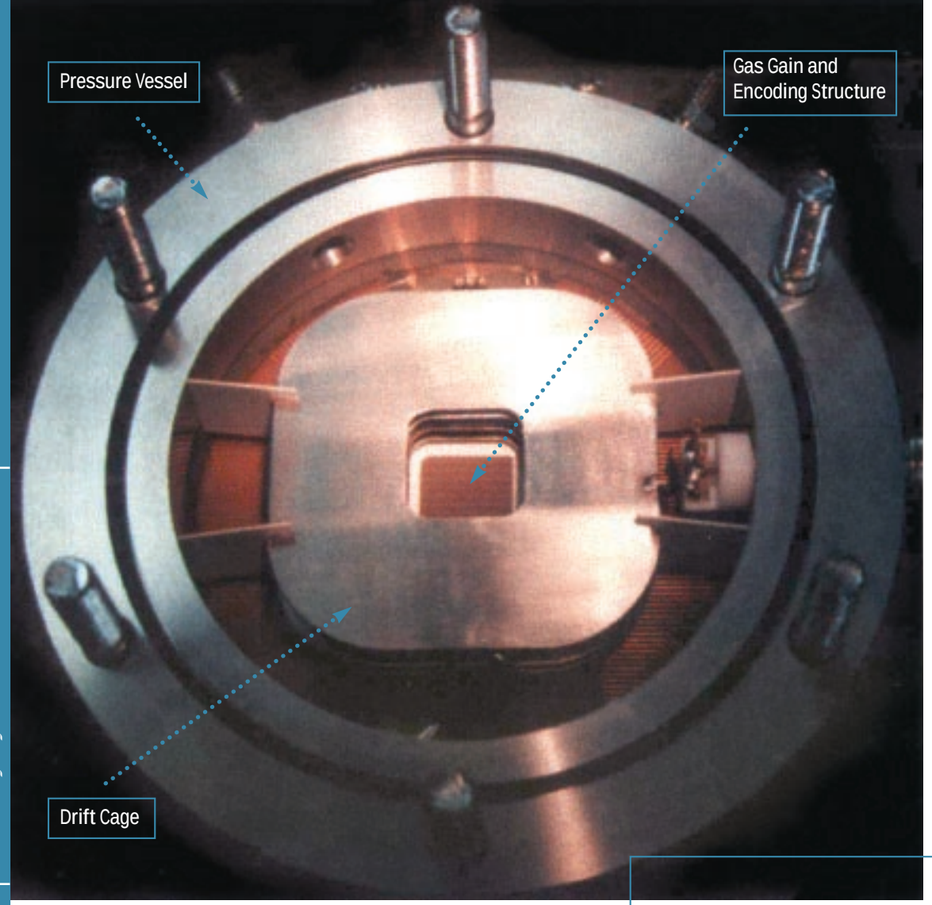

FIGURE 1

Photograph of the opened 2D detector. The inner diameter of the pressure vessel is 120 mm. At the bottom of the drift cage the gas gain and encoding stage are visible (active area 28 x 28 mm^2). The photons penetrate into the detector from the top (through an carbon entrance window which is not shown here) and are absorbed by the gas within a drift depth of 20 mm.

In a close collaboration between the detector laboratories of the Sincrotrone Trieste and that of the Department of Physics, University Siegen, two gaseous prototype detectors suitable for the aforementioned applications in the energy range between 5 keV and 16 keV were developed. Both state-of-the-art detectors feature a high quantum efficiency (more than 70%) that can be adjusted by the appropriate gas mixture and the gas pressure (up to 5 bars) and a spatial resolution of about 200µm. The first one is a one dimensional integrating detector (in the following called '1D' (for a detailed description see Menk *et al.*, 1998)) and the other is a two dimensional single photon counting pixel detector (in the following called '2D' (Besch *et al.*, 1997)) (figure 1). Besides an extraordinary global count rate of some hundred MHz the 2D has an impressive time resolution in the sub micro second range which in principle is only limited by the single photon signal development in the conversion gas. The 1D features a huge and unique dynamic range (10^8 with single photon resolution) at moderate read out times (some hundred µ-seconds). Both systems are equipped with a novel gas gain structure, namely the Micro-CAT, which performs a charge amplification of the primary electrons by factors between 1 and 10^4. The working principle of this structure is based on a strong increase of the electrical field in the vicinity of micro-holes and is very similar to that of other gas gain structures which have been developed in the past 5 years, such as CAT (Bartol *et al.*, 1996), MICROMEGAS (Giomataris *et al.*, 1996) or GEM (Sauli, 1997). The 1D records the deposited charge by charge integration. In this case the gas gain mechanism is used to adjust the total charge in the detector according to the incoming pho-

FIGURE 2

Diffraction pattern of the rat tail tendon collagen recorded with the 1D with variable gas gain. The region close to the beam stop was imaged with ionization chamber mode while the 8th order was measured with a gas gain of 10000. The high voltage discharges (signed as HV sparks) occurred seldom (1 per minute or even less) and can be clearly distinguished from the diffraction peaks.

ton flux, so that for each single photon a signal is always generated which is significantly higher than the noise background of the integrating electronics. Hence, for almost all photon fluxes single photon precision can be obtained. The 2D is operated in single photon counting mode. Here the gas gain mechanism is used, to obtain the maximum intensity precision. Although the amplification structure is similar, the position encoding differs for both devices. In the case of the 1D, position resolution is obtained by collection the deposited and optionally amplified charge on a fine structure with gold-plated parallel strips while 2D provides a two dimensional position resolution by local interpolation within resistive cells. At the four corners of such a cell read-out nodes are placed and connected with low impedance amplifiers. From the different signal amplitudes at the four nodes the position of the hit can be calculated.

Both detector systems have been tested in a series of synchrotron radiation measurements with monochromatic 8 keV radiation delivered by the SAXS station at the Sincrotrone Trieste (Amenitsch et al. 1998; Bernstorff *et al.*, 1998) evaluating all parameters which are essential for advanced diffraction applications. Utilizing a dynamic adjustment of the gas gain during a detector scan it was possible to measure almost the entire diffraction pattern of a rat tail tendon collagen sample from the 8^{th} order peak to a region very close to the direct beam featuring a dynamic range of 10^7 –10^8 which is unique for imaging detectors so far (Fig. 2). The single photon read out and storage of the 2D yields an excellent time resolution. In order to demonstrate this feature a time dependent biological process has been recorded. Here the time resolution was utilized to record diffraction pattern of a protein crystal, that was rotated with constant angular velocity, with a time resolution of 18 µs which is equivalent to a very fine angular slicing of 0.001°. This procedure enables a precise determination of the narrow rocking curve of selected diffraction spots (see Fig. 3), which generally increases the precision of spot intensities and thus the quality of the reconstructed object.

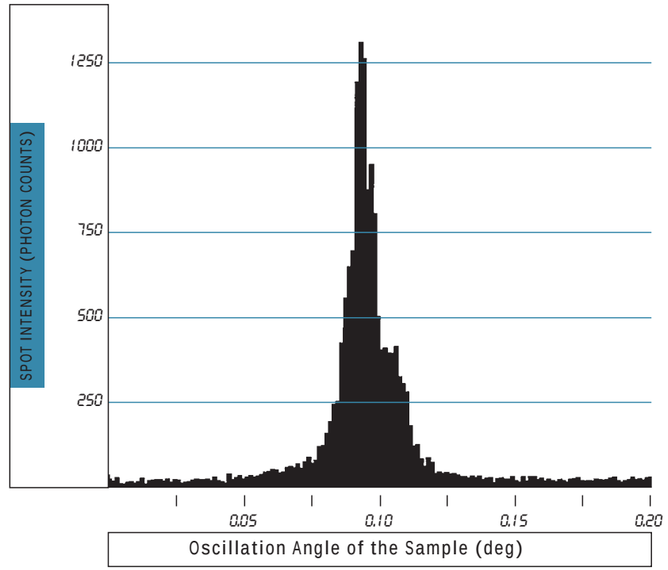

FIGURE 3

Rocking curve of a diffraction spot (at 41.4 Å resolution) from a medium size protein crystal (unit cell: a = 53.3 Å, b = 72.5 Å, c = 72.8 Å; space group: $P2_12_12_1$); the data have been derived by cutting the continuously recorded pattern in angular slices of 0.001° width.

REFERENCES *[1] Amenitsch, H., Rappolt, M., Kirchbaum, M., Mio, H., Laggner, P. & Bernstorff, S. (1998). J. Synchrotron Rad. 5, 506-508.*
[2] Bartol, F., Bordessoule, M., Chaplier, G., Lemonnier, M. and Megtert, S. (1996). J. Phys. III France 6, 337.
[3] Bernstorff, S., Amenitsch, H. & Laggner, P. (1998). J. Synchrotron Rad. 5, 1215-1221.
[4] Besch, H. J., Junk, M., Meißner, W., Sarvestani, A., Stiehler, R. & Walenta, A. H. (1997). Nucl. Instr. and Meth. A 392, 244-248.
[5] Giomataris, Y., Rebourgeard, Ph., Robert, J.P. and Charpak, G. (1996). Nucl. Instr. and Meth. A376, 29.
[6] Helliwell, J. R., Ealick, S., Doing, P., Irving, T. & Szebenyi, M. (1993). Acta Cryst. D 49, 120-128.
[7] Kriechbaum, M., Rapp, G., Hendrix, J. & Laggner, P. (1989). Rev. Sci. Instr. 60, 2541-2544.
[8] Menk, R. H., Arfelli, F., Bernstorff, S., Pontoni, D., Sarvestani, A., Besch, H. J. & Walenta, A. H. (1998). Nucl. Instr. and Meth. A 422, 698-703.
[9] Sarvestani, A., Besch, H. J., Junk, M., Meißner, W., Sauer, N., Stiehler, R., Walenta, A. H. & Menk, R. H. (1998a). Nucl. Instr. and Meth. A 410, 238-258.
[10]Sauli, F. (1997). Nucl. Instr. and Meth. A386, 531.

Facts and Events








2nd Open-House at Elettra
17-18 October 1998
(more than 6 thousand visitors, coming from all over Italy, Slovenia, Croatia, Austria)






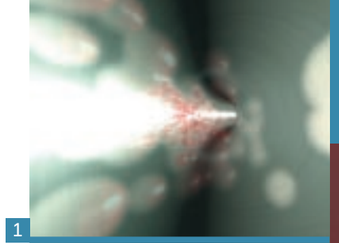

1

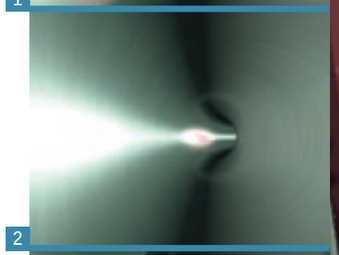

2

3

Some Images from the Elettra Health Physics and Safety Video Clip

1

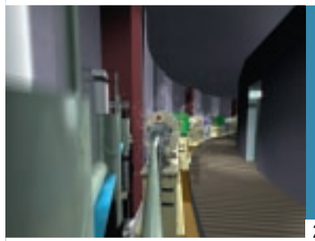

2

3

6th Elettra Users' Meeting
30 Nov - 1st Dec 1998

Beamline Status

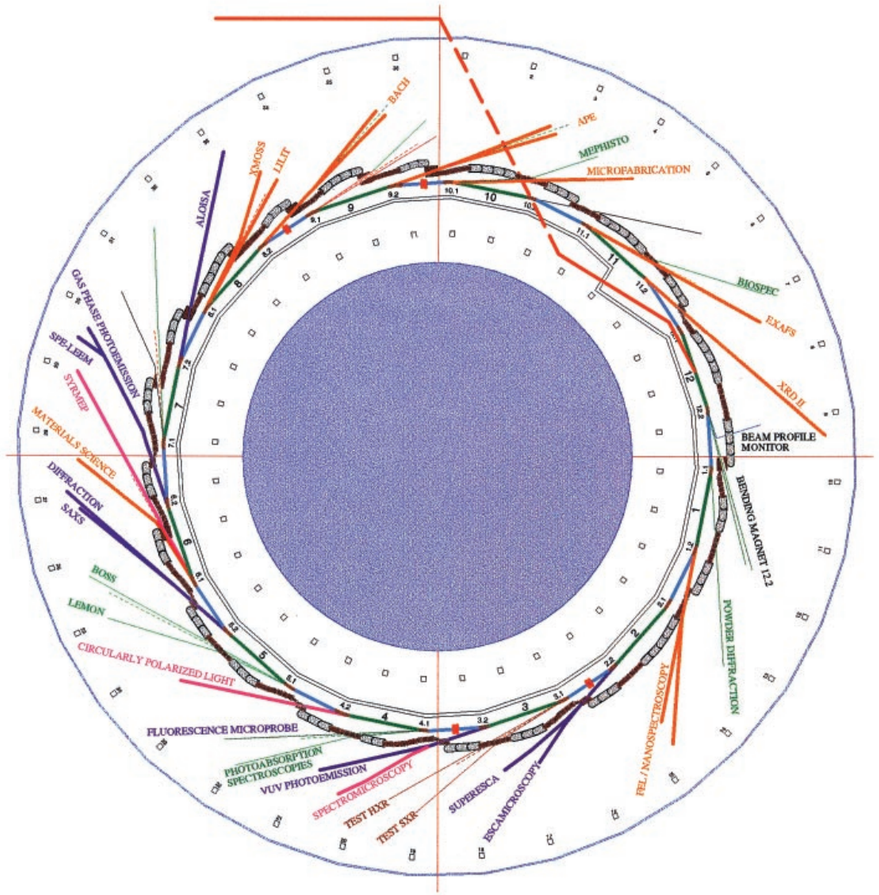

STATUS: OPERATIONAL

N°	Beamline	RT's Institution	Photon Source	User Oper.
1	SuperESCA	Sincrotrone TS	Undulator U5.6	Mar 95
2	ESCAMicroscopy	Sincrotrone TS	Branch Line of N°1	Jun 95
3	VUV Photoemission	CNR-ISM	Undulator U12.5	Jun 95
4	X-ray Diffraction	CNR	Wiggler W 14.0	Jun 95
5	X-ray Small-angle Scattering	Austrian Academy of Sciences	Branch Line of N°4	Sep 96
6	Surface Diffraction (ALOISA)	(CNR) INFM	U 8.0 Undulator/Wiggler	Jan 98
7	Gas-Phase Photoemission	CNR-IMAI INFM Univ. of Rome	U 12.5 Undulator	Jan 98
8	SPE-LEEM	University of Clausthal	Branch Line of N° 7	Jan 98
9	Mammography (SYRMEP)	University of Trieste-INFM	Bending Magnet	Jan 98
10	Spectro-Microscopy	Sincrotrone TS-EPFL-CXRL	Branch Line of N° 3	Jan 98

STATUS: UNDER COMMISSIONING

N°	Beamline	RT's Institution	Photon Source
11	Circularly Polarized Light	CNR-ISM CNR-ICMAT Univ. of Rome I	Cross Field Undulator/Wiggler

STATUS: APPROVED BY SAC AND CdA UNDER CONSTRUCTION

N°	Beamline	RT's Institution	Photon Source
12	EXAFS	Univ. of Trieste	Bending Magnet
13	Microfabrication	Sincrotrone TS	Bending Magnet
14	Materials Science	Czech Academy of Sciences - Prague	Bending Magnet
15	Beamline for Advanced Dichroism (BACH)	INFM	Cross-Field Undulator
16	Dichroich Photoemission (APE)	INFM	Cross-Field Undulator
17	Soft X-ray Optical Spectroscopy (X-MOSS)	INFM	Bending Magnet
18	Proximity Photolithography (LILIT)	INFM	Bending Magnet
19	XRDI II	Sincrotrone TS	Wiggler
20	Nanospectroscopy	Sincrotrone TS	FEL Undulator
21	Powder Diffraction	CNR-Univ. of Trento	Bending Magnet
22	Inelastic Ultraviolet Light Scattering	Sincrotrone TS	Undulator

STATUS: PROPOSED

N°	Beamline	RT's Institution	Photon Source
23	Miniundulator	CNR	Undulator
24	BIOSPEC	CNR	Bending Magnet
25	MEPHISTO	CNR	Bending Magnet
26	Photoabsorption Spectroscopies	CNR	Bending Magnet
27	Low Photon Energy High-Resolution Photoemission (LEMON)	CNR	Bending Magnet
28	Multipurpose X-ray Beamline (BOSS)	J. Stefan Institute Ljubljana	Bending Magnet
29	Fluorescence Microanalysis	Sincrotrone TS	Bending Magnet
30	Soft X-ray Test BL	Sincrotrone TS	Bending Magnet
31	Hard X-ray Test BL	Sincrotrone TS	Bending Magnet

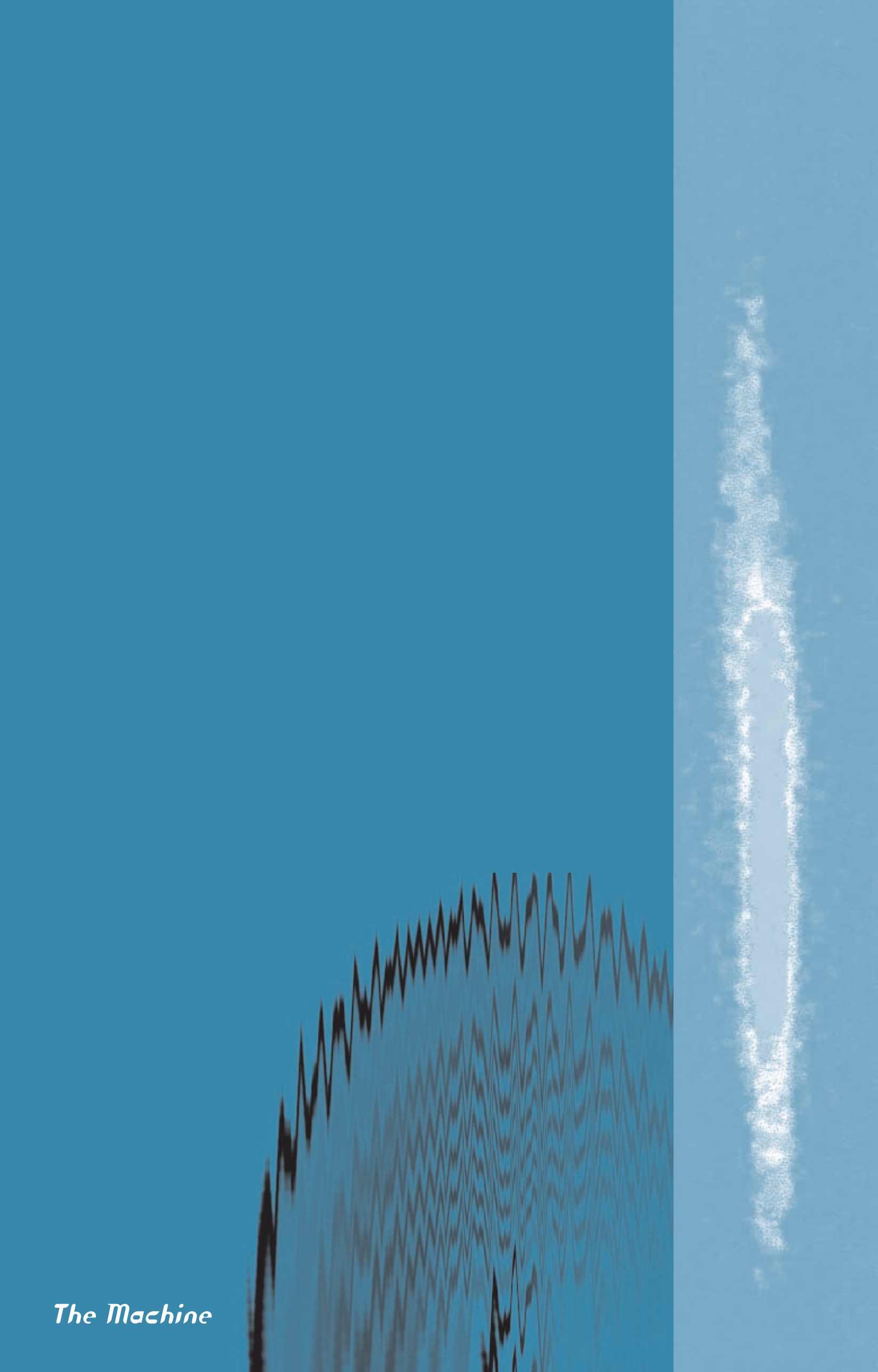
The Machine

Operations

At the end of 1998 ELETTRA completed five years of operation for the User community. Over this period the facility operated for more than 27,000 hours of which more than 20,000 were dedicated to User experiments. Last year the facility operated for the greatest number of hours, a total of 6528 of which 5256 were dedicated to User operation. The operating hours of 1998 were distributed over six runs of continuous 24 hour/day light source operation. The runs had a duration of six to eight weeks, interrupted by three short (one week) and two long (four week) shutdown periods. Machine study periods (one to three days) for the optimisation of accelerator performance and component conditioning took place approximately every seven to twelve days throughout the runs. Normal operation for Users involved one refill per day with a starting beam current of 315 mA (7 hrs lifetime) at 2.0 GeV that decayed to ~100 mA (35 hrs lifetime) after 24 hours. Figure 1 shows the lifetime as a function of current for the 1998 operating conditions. The scheduled operations calendar for 1999 is less dense (6192 hours) and reflects the large number of installations to be made on the machine. Operations during 1999 will be performed during eight runs of five to eight weeks, with nine shutdown periods of one to three weeks. The more frequent shutdowns will be used for the installation of new front ends, vacuum chambers and insertion devices for new beam lines and for strategic upgrades to improve the performance of the accelerator.

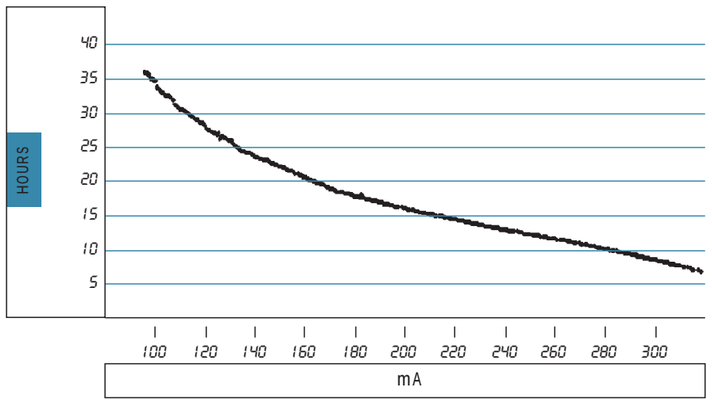

FIGURE 1

Typical plot of lifetime as a function of current following daily refill of 315 mA at 2.0 GeV at 09:30.

The operations efficiency for 1998 (for each run) is shown in figure 2. The annual uptime for the User runs was 92.6%. The overall User uptime, excluding external disturbances, such as thunderstorms and power fluctuations, was 93.6%. Storms accounted for a significant fraction of User downtime (0.95% of run time). Other major sources of downtime were cooling water plants (1.4%) and power supplies (0.73%). The totalled five-year uptime exceeded 93%.

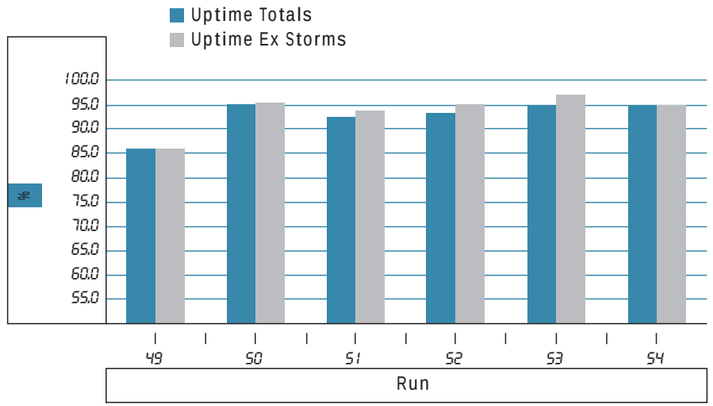

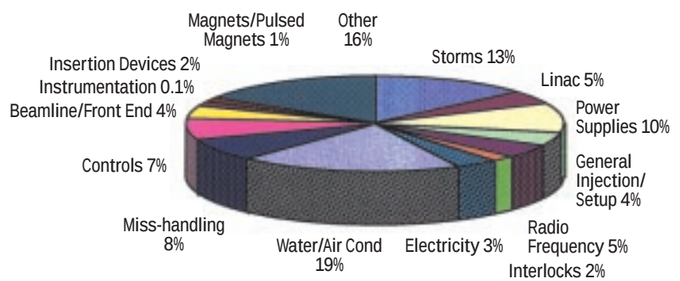

FIGURE 2

1998 User Uptime and sources of User downtime.

Extensive studies and machine shifts were dedicated throughout the year to determine the maximum operating energy of the light source. Consideration of the thermal load on the vacuum chamber, beam stability, radio frequency requirements and the efficiency of orbit correction were taken into account. The findings gave a top energy of 2.46 GeV. The Users were then given the possibility of experimenting with a 2.4 GeV beam and 120 mA. The experience was highly positive and led to assigning 23% of the first semester of 1999 User shifts to operation with a beam energy of 2.4 GeV. The current is limited to 120 mA to contain the thermal load on the vacuum chamber at acceptable values. The lifetime, strongly limited by the Touschek effect at the lower energies, is 52 hours at 100 mA compared to 32 at the same current at 2.0 GeV.

Since ELETTRA does not have a full energy injector the beam has to be energy ramped in the storage ring. This leads to an estimated 2-3% average efficiency loss directly connected to up-time. In addition accelerator component failures are noticeably linked to changes made to the machine state. In view of this improvements were made to the automatic refill program manager '1bm' to perform a reduced magnet cycling. Further improvements include the addition of modules for the automatic control of machine shutters and valves, control and setting of the final orbit and the initial setting of insertion device gaps.

Although there are no official requests for single bunch operation Users are increasingly interested in few bunch filling modes. Due to the low machine impedance relatively high currents per bunch can be stored. The machine can be flexibly used and any filling structure can be made including bunch distributions such as half the ring continuously filled accompanied by a single bunch in the empty other half. Users performed measurements with 6 and 12 equidistant bunches with 10 mA/bunch and took spectra as well as performed time of flight experiments. Figure 3 shows a spectrum taken with 6 bunches and in multibunch mode. Operation with a small number of bunches increases the chance of mode self-cancellation. This happens when a coupled bunch mode samples the Higher Order Modes (HOM's) of the cavities in such way that the sum of the growth rates over all HOM's becomes negative or zero. After careful tuning of the temperature of the cavities longitudinal mode cancellation has been observed for 6 and 18 bunches at 2.0 GeV, but most important for 4 equidistant bunch operation at 1.0 GeV with a total current of 100 mA. This later mode is particularly important for operation of the storage ring FEL at 1.0 GeV. In Figure 4 the break down of the cancellation is shown when four bunches with the same total current were injected.

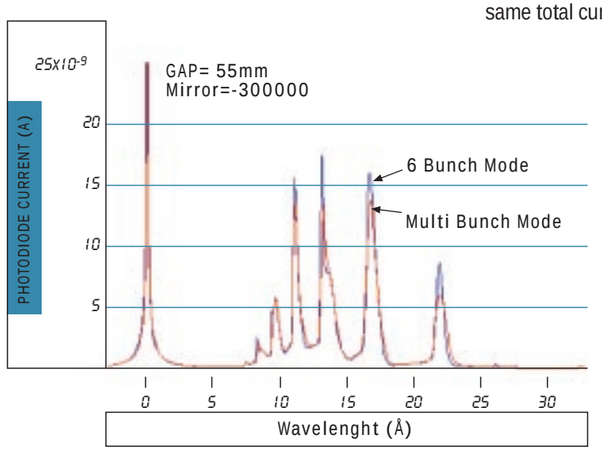

FIGURE 3

Spectra at 2 GeV for 6 bunches and a multibunch filling pattern taken by Aloisa users during a June 1998 shift with the insertion device set at a gap of 55 mm.

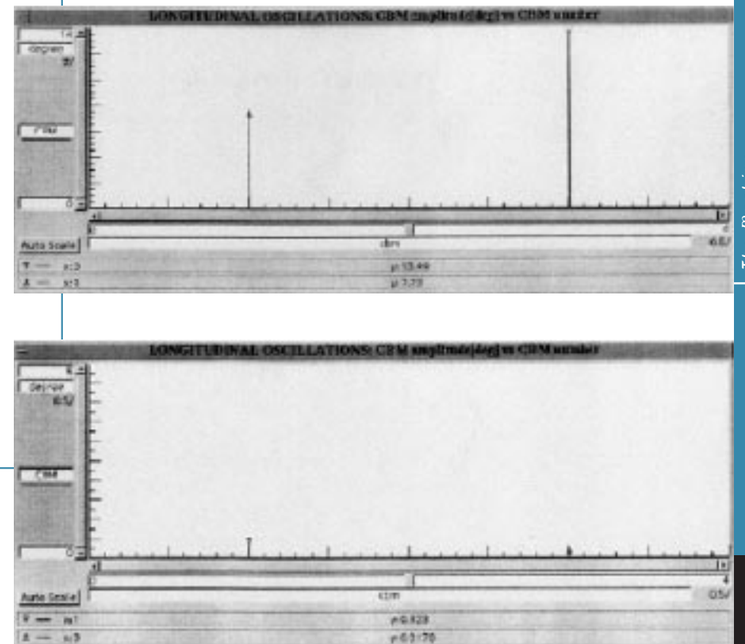

FIGURE 4

Intensities of longitudinal coupled bunch oscillations in the four bunch mode at 1.0 GeV. The upper picture shows the longitudinal spectrum where the coupled bunch modes 1 (8°) and 3 (13.5°) are excited by HOMs. The lower picture shows the same modes when mode cancellation occurs (both modes are below 0.5°); one degree of phase motion corresponds to an oscillation amplitude of 5.5 ps.

A streak camera was added to the arsenal of beam diagnostics at ELETTRA in November. The instrument allows measurement of the bunch length and the camera is equipped with different time-bases that allow various operational modes; single sweep (with 2 ps resolution), dual sweep (two linear sweeps) and dual sweep with synchroscan. A main feature of a Streak Camera is the capability of providing pico-second resolution during a single acquisition without any averaging. The synchroscan frequency of 250 MHz allows the unique capability of observing consecutive bunches spaced 2 ns apart. The camera will be used to provide information on the quality of the beam and its parameters and permits accurate calibration of other equipment used for routine observation and control.

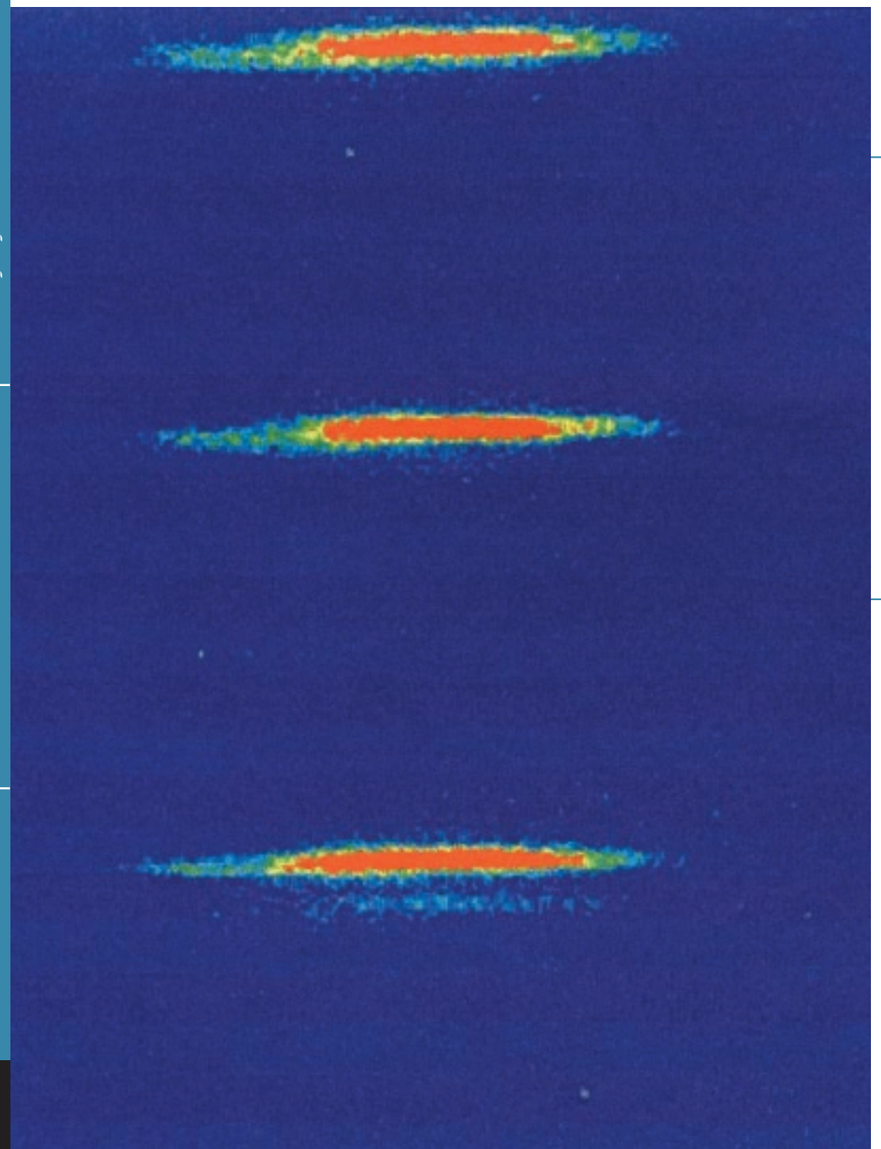

FIGURE 5

Dual sweep streak camera synchroscan image of a single bunched beam over three consecutive turns (864 ns per turn). The electron distribution has a measured full width half maximum of 60 ps.

A novel Electromagnetic Elliptical Wiggler (EEW) was installed at the beginning of January '98 as a source of circularly polarised radiation for a new beam line. First light was provided in February followed closely by the first polarisation measurements in April. The main feature of this device is the possibility of switching the helicity of the radiation in either a trapezoidal (0.1-1 Hz) or sinusoidal mode (10-100 Hz). The principal influence on the beam observed during the commissioning of the device was a change in the closed orbit. A correction system consisting of air-cored coils and arbitrarily programmable power supplies were put successfully in operation the DC mode. Correction of the AC mode will be implemented in 1999.

To enable Users to synchronise beam and acquisition signals a project was initiated during the year to provide comprehensive distribution of timing signals from storage ring radio frequency clocks. The work will be completed in 1999.

Recabling of the transfer line dipole magnets was completed enabling use of only the first part of the transfer line for linac diagnostics. This avoids disturbance and subsequent correction of the stored beam closed orbit.

During the year the machine was operated by a single person who was provided with extensive backup in case of component failure. To further improve the efficiency of machine recovery, after component failure, an operations team of seven people was formed in November. The team is fully dedicated to the operation of the accelerators and will provide assistance during shutdown periods. Operation for 1999 will proceed with two people, the second person taken from the pool of people making up the accelerator sector who will provide assistance to operations and by doing so will maintain contact with machine operation.

New Sources of Photons

The increased demand of the User community to have polarised radiation from insertion devices is being satisfied by the construction of new APPLE type undulators having four arrays of permanent magnets (NdFeB). Six new insertion device modules for three straight sections were under various stages of design during the year for forthcoming beam lines: APE, BACH and FEL/nanospectroscopy (see table 1). All of these will be APPLE-2 type devices in order to provide horizontal, circular and vertical photon polarisation. All previous insertion devices (apart from the EEW) were based on a standard 1.5 m long support structure, and in most cases three such modules were accommodated in each straight section. These new devices will be split into two sections rather than three and are based on a 2.0 to 2.2 m long standard support with integrated phase motion for polarisation adjustment. The first 6 cm period device, for the APE beam line, has been assembled and shows good agreement between measured field distributions and model calculations. A second device (12.5 cm period), also for the APE beam line, will be a novel quasi-periodic variably-polarised device that will limit as far as possible contamination from higher order harmonics that are difficult to filter by optical methods.

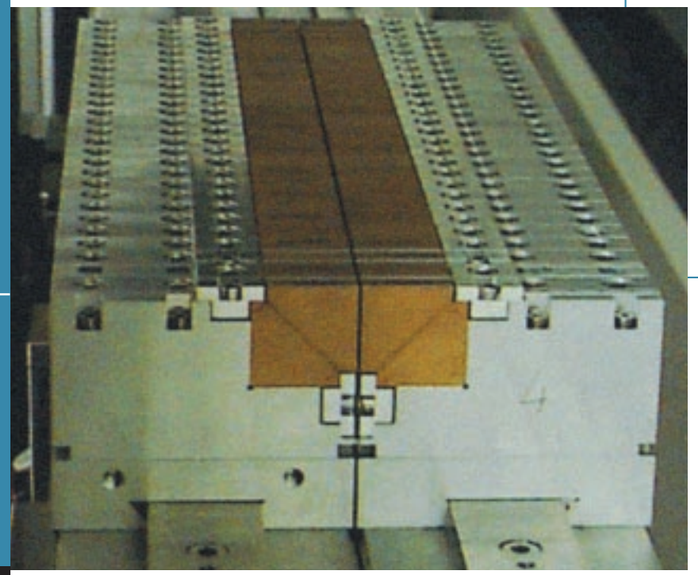

FIGURE 6

Lower half of an undulator prototype for polarised radiation.

FIGURE 7

Schematic of the new variable polarisation quasi-periodic undulator.

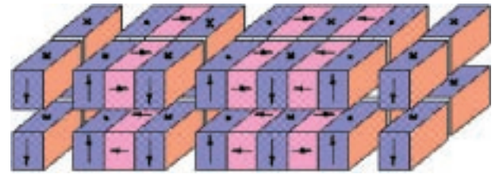

The above two mentioned insertion devices will be installed in one straight section separated by a chicane magnet thus enabling two experimental stations to be operated simultaneously. The undulators of length about 2.2m are separated by a small dipole magnet that will provide a 2 mrad separation of the two photon beams. For the storage ring FEL project two identical undulator segments, together with a phase modulation electromagnet, will be used in an optical klystron configuration.

TABLE 1

Existing and planned Insertion Device parameters

BEAMLINE	ID#	TYPE1	N	GAP (MM)	BO (T)	K
Operational Devices:						
• SuperESCA • ESCA microscopy	2	U5.6	81	27.0	0.44	2.3
• VUV photoemission • Spectromicroscopy	3	U12.5	36	28.0	0.51	5.9
• Circular Polarization	4	EEW21.2[2]	15	18.0	0.1/0.5	1.5/10
• X-Ray diffraction • Small angle scattering	5	W14.0	30	22.0	1.50	19.6
• Gas phase photoemission • SPE-LEEM	6	U12.5	26	26.0	0.55	6.4
Devices under construction:						
• FEL • Nanospectroscopy	1	EU10.0[3]	40	18.0	0.62/0.78/1.01	5.9/7.3/9.5
• BACH	8	EU4.8[3] EU7.7[3]	44 28	18.0 18.0	0.29/0.33/0.57 0.53/0.65/0.91	1.3/1.5/2.6 3.9/4.7/6.6
• APE	9	EU6.0[3] EU12.5[3]	36 17	18.0 18.0	0.42/0.51/0.78 0.47/0.60/0.78	2.4/2.9/4.4 5.5/7.0/9.1
• X-Ray Diffraction-II	11	in phase of definition				

Notes: 1 type: U-undulator, W-wiggler, EEW-electromagnetic elliptical wiggler, EU-elliptical undulator; the following number gives the period length in cm.
2 maximum horizontal and vertical field strengths respectively 3 maximum circular, vertical, and horizontal fields respectively

The intense activity in constructing new beam lines is also seen in the fabrication of new front ends. In addition to the placement of orders for two front ends for insertion device beam lines (APE and the second crystallography beam line), three orders were also placed for the construction of bending magnet front ends. The first of which arrived at the end of the year ready for the LILIT/X-MOSS beam line. In addition the front end serving the FEL/nanospectroscopy beam line is being assembled in house.

FIGURE 8

Bending magnet front end showing the two beam extraction pipes.

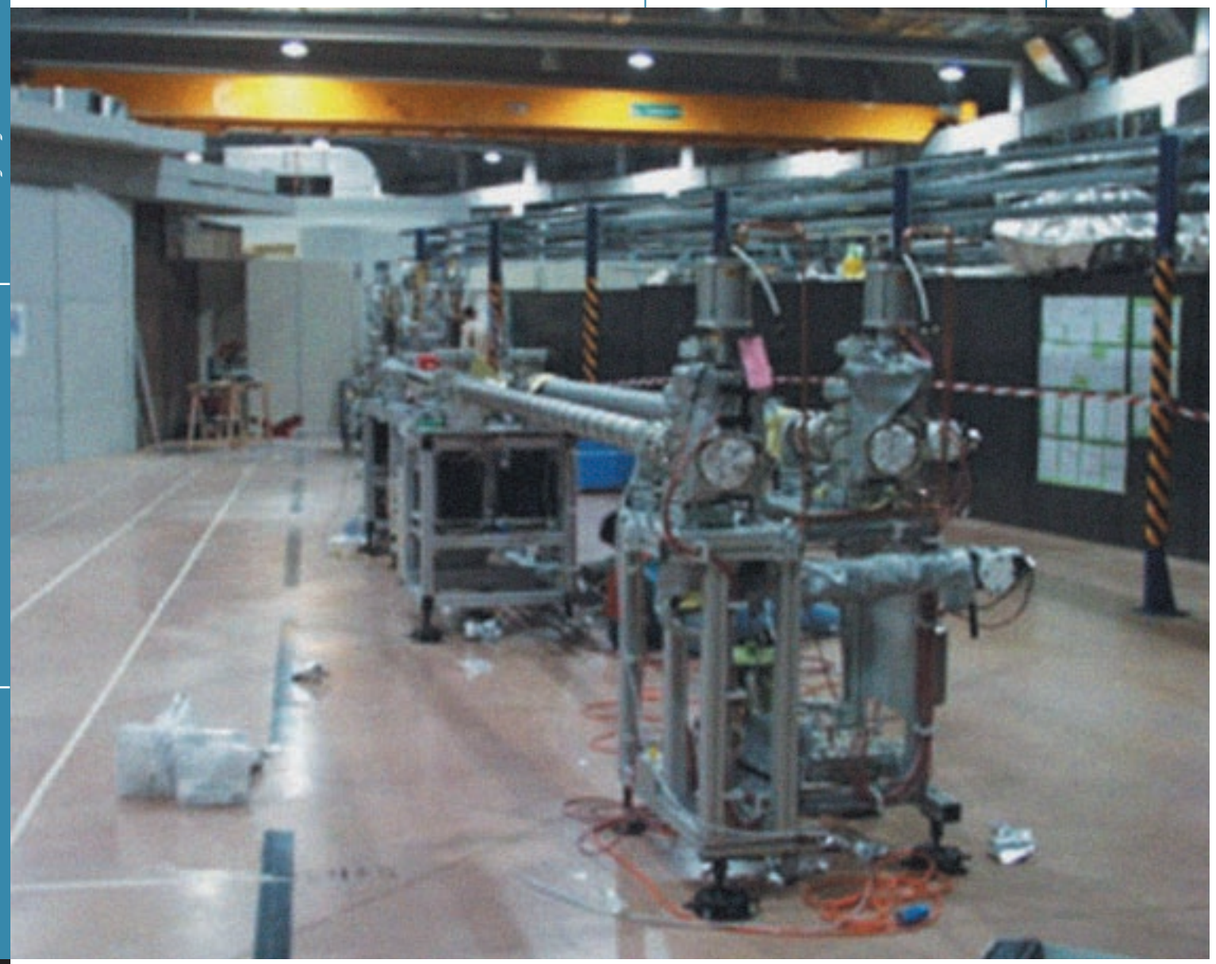

The installation of new insertion devices providing horizontal, circular and vertical polarised synchrotron radiation has called for the development of new bending magnet vacuum chambers to account for the increased thermal load on the radiation slot. The chambers made of aluminium alloy AlMg-Mn (Peraluman) have high thermal conductivity and are greatly simplified compared to the original stainless steel types. The main differences being the absence of an internal NEG strip and the removal of the photon beam stopper away from the chamber body. This has allowed a more compact form and minimised chamber deformation in addition to easing upgrades of the photon beam shutter whenever higher power densities are encountered from new insertion devices.

In addition to the bending magnet chambers, extruded aluminium vacuum vessels are now being adopted for all future and some existing insertion devices. These ID chambers are pump-free with an elliptical cross-section that has a minimum internal aperture of 14 mm and an external dimension of 17 mm. These economical chambers are easy to manufacture and have cooling channels on either side. The same technique will also be adopted for those parts of the machine having a rhomboidal cross-section.

The first set of bending magnet and insertion device chambers of the APE beam line was installed in October. The existing Super-ESCA/ESCA-microscopy beam line will have a new extruded insertion device chamber installed in the summer of 1999.

FIGURE 9

The first low gap extruded aluminium insertion device vacuum chamber installed in section 9.

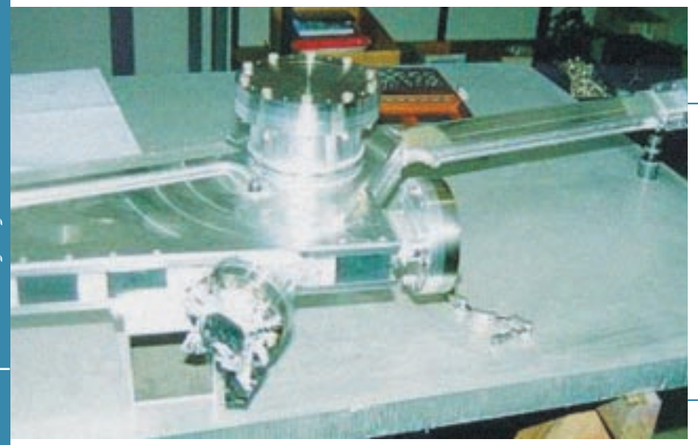

FIGURE 10

Details of the new aluminium bending magnet chamber, showing beam pipe and photon port.

A three year research and technological development (RTD) project started in May funded by the European Commission under its program for improvements to Large Scale Facilities, for the development of a UV/VUV storage ring free electron laser (SR-FEL) on ELETTRA. The other partners in the project are CEA/LURE, CLRC-Daresbury Laboratory, University of Dortmund, ENEA-Frascati and MAX-lab. The aims of the project are related to the potential use of the FEL as a user facility, i.e. stable lasing over a broad range, at least between 350 and 190 nm, while still permitting the operation of other synchrotron radiation beam lines. Initial operation will be at 1 GeV, although higher energy operation will also be explored. Recent tests of storage ring performance in a FEL mode (1 GeV, 4-bunches) have given the encouraging results that stable operation with 100 mA total current can be achieved with a peak current of the order 200 A. Design and construction of all major components has started and installation is planned between August and October 1999. First lasing attempts will be made towards the end of 1999 at 350 nm before proceeding towards shorter wavelengths (<200 nm).

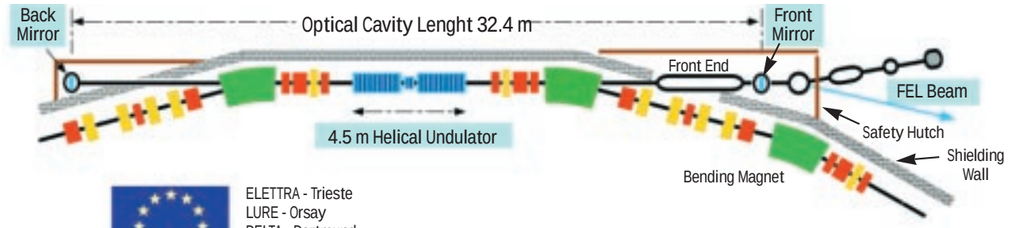

ELETTRA - Trieste
LURE - Orsay
DELTA - Dortmund
CLRC - Daresbury
ENEA - Frascati
MAX-LAB - Lund

FIGURE 11

Schematic diagram of the Storage Ring Free Electron Laser layout.

The beam line construction plan has already allocated ten insertion devices to the eleven possible long straight sections. The last remaining section will be allocated in 1999. Attention has therefore turned to the two short (1.2-1.5 m) sections in each achromat of the expanded Chasman-Green structure making up the storage ring lattice. Much of this space has already been put to good use by placing diagnostics and the radio-frequency cavities there, however even without moving existing diagnostics nine locations are available. Machine operation with such devices has been studied and appears to be possible with certain restrictions. Beam sizes and divergences are larger than for standard insertion devices and there is a greater sensitivity to energy spread variations. Linear optics effects on tunes, beta functions and dispersion are acceptable provided many high field devices are not installed. No further deterioration in dynamic aperture is expected above that introduced by the existing devices. Effects on emittance are not great, but may limit the field of any high field tuneable devices to prevent intensity fluctuations on other beam lines. Flux and brightness calculations for representative devices indicate 20 times better flux from a wiggler and 200 to 300 times more brightness from an undulator compared to the bending magnet sources. In view of the strong interest in such sources a first bending magnet chamber (in aluminium) will be constructed in 1999 to allow the extraction of radiation at both 0° (ID) and 3.45° (bending magnet). The insertion device itself will be the subject of study in the coming year. With minor modifications a standard bending magnet front end will be adopted.

Machine Developments

Longitudinal instabilities are successfully controlled in ELETTRA by means of a precise adjustment and regulation of the temperature of the radio-frequency cavities. To provide an extra degree of freedom, variable plungers (higher order mode frequency shifters) have also been installed in two cavities. At the present time the cavity settings are adjusted so as to leave a residual longitudinal excitation, in order to provide an increase in beam lifetime as well as to overcome transverse effects which arise when the beam is completely stable longitudinally. Complete control of both longitudinal and transverse instabilities by cavity temperature tuning is possible but is laborious to perform and becomes increasingly more difficult to do at higher currents. Since longitudinal stability is desirable in order not to deteriorate undulator radiation spectra, particularly in the future when the use of higher harmonic numbers are foreseen, another method is needed to guarantee transverse stability. For this reason a transverse feedback is under development. The feedback is a wideband bunch by bunch system where the positions of the 432 bunches, separated by 2 ns, are individually sampled and corrected. In order to damp the oscillations of a bunch, the amplitude of the correcting kick must be proportional to the slope of its trajectory at the time it passes through the kicker. The slope is determined by detecting and adequately processing the bunch position signal measured one or few turns before (revolution period 864 ns).

The block diagram of the transverse multibunch feedback for one of the two transverse planes is shown in figure 12. Programmable Digital Signal Processor (DSP) based electronics is being used for the processing block giving a very high level of flexibility. Beside providing the right phase between the Beam Position Monitor (BPM) and the kicker signals different types filter can be run on the DSPs. Furthermore, suppression of the DC closed orbit component, optimisation of the needed power, accounting for changes in machine operating conditions (tune, current, etc.), saturation control and system diagnostics can easily be performed. The adopted design will allow use of the same digital processing hardware on different machines and/or for longitudinal multibunch systems. The Swiss Light Source is a collaborative partner in this project contributing to the design of the kickers and electronics of the monitor.

A software simulator has been developed to study the behaviour of the system for different machine conditions, BPM and kicker positions, digital filters, etc. Figure 13 shows the simulated damping effect of the feedback on the amplitude of the multibunch oscillations observed by the Beam Position Monitor. The first complete system tests are foreseen for autumn '99.

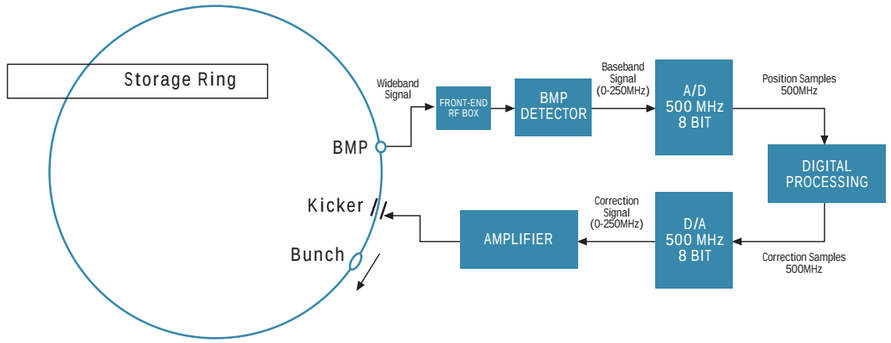

FIGURE 12

Transverse Multibunch Feedback System layout.

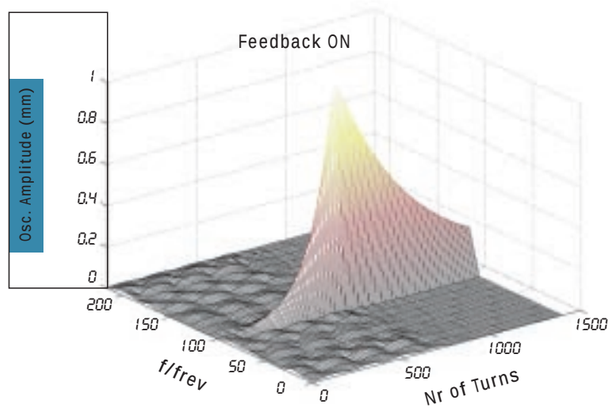

FIGURE 13

Simulated TMBF damping effect of the multibunch oscillation amplitudes vs. number of turns observed by the Beam Position Monitor.

The operation of the transverse multibunch feedback together with an appropriate tuning of the cavity temperatures to eliminate longitudinal instabilities will give an electron beam of the highest quality. The subsequently reduced effective emittance will also lead to a reduction in lifetime. To increase the lifetime a bunch lengthening third harmonic cavity is being considered. The first stage of assessment and study of a superconducting option was completed during the year. The cavity will be a scaled version of the double cell system proposed for the SOLEIL project. The idle cavity will operate at 1.5 GHz and provide a maximum voltage of 600 kV. Beam energy losses of a few Watts are easily replaced by the active 500 MHz system. The improvement to the lifetime (Touschek) is of the order of a factor of 3 to 3.5 at 2.0 GeV and 2 to 2.5 at 2.5 GeV.

Photon beam stability is of paramount importance for a light source. A lot of effort has been put into developing new diagnostic tools for determining the position of the photon source point. This effort has been directed towards the development of both photon beam position monitors (pBPM's) and electron beam position monitors (eBPM's).

The new electron BPM system is at an advanced stage of design and will provide ultra-stable position signals, at the mm level, for a local feedback processor. The eBPM has been designed for the low gap aluminium chambers mentioned above. In order to achieve the expected performance, two main developments have been undertaken: a mechanical design of a low gap BPM fitted with 14mm diameter buttons along with the relative support system and vacuum chamber interface and an electronic design that includes a new analog front-end and a digital amplitude demodulator. For maximum sensitivity in the vertical plane the buttons have been located close together with only 12mm center-to-center distance in the horizontal plane. Two bellows, either side of the BPM body, will isolate mechanical movement transmitted by the vacuum chamber. The support system will provide state-of-the-art short-term (vibrations) and long-term (thermal) stability to the monitor. Furthermore a monitoring of BPM motion at the sub-mm level will be installed using either an opto-electronic micrometer or capacitive sensors.

In designing the BPM electronics the latest state-of-the-art electronics has been used, especially from the rapidly growing telecommunications industry. The electronic processing has to provide high-stability and resolution for the button signals with sufficient bandwidth for a local feedback system to operate properly. The electronics of the BPM system is composed of an analog front-end, a digital receiver (AM demodulator) and a DSP processor. Both parallel four button and multiplexing front end signal processing is being developed. The digital receiver will provide horizontal and vertical position signals by means of a Digital Demodulator (Digital Down-Converter). The DSP module will manage the data stream and provide filtered values to the central processor of the local feedback. Two new eBPM's will be installed in an insertion device straight of an existing beam line in late summer next year.

Recent developments with new pBPM's have concentrated on solving the problem of the contamination of the insertion device radiation with that of the up- and downstream bending magnets. A direct consequence of the contamination is an overall change of the distribution of photons intercepted by the monitor when a insertion device gap change is made. This is interpreted as a fictitious movement of the photon beam and consequently of the electron beam. To overcome these limitations studies have been made of new kinds of pBPM's that perform an energy analysis of the photo-electrons emitted in the monitor when hit by the photon beam. This allows to distinguish the higher energy photons from the insertion device compared to those of the bending magnet fringe field. The design and construction of a test chamber has been initiated to test the new concept. The chamber containing two intercepting blades and corresponding electron energy analysers, constructed in collaboration with the INFM, will be mounted on an existing beam line in 1999.

Elettra Highlights
The Machine

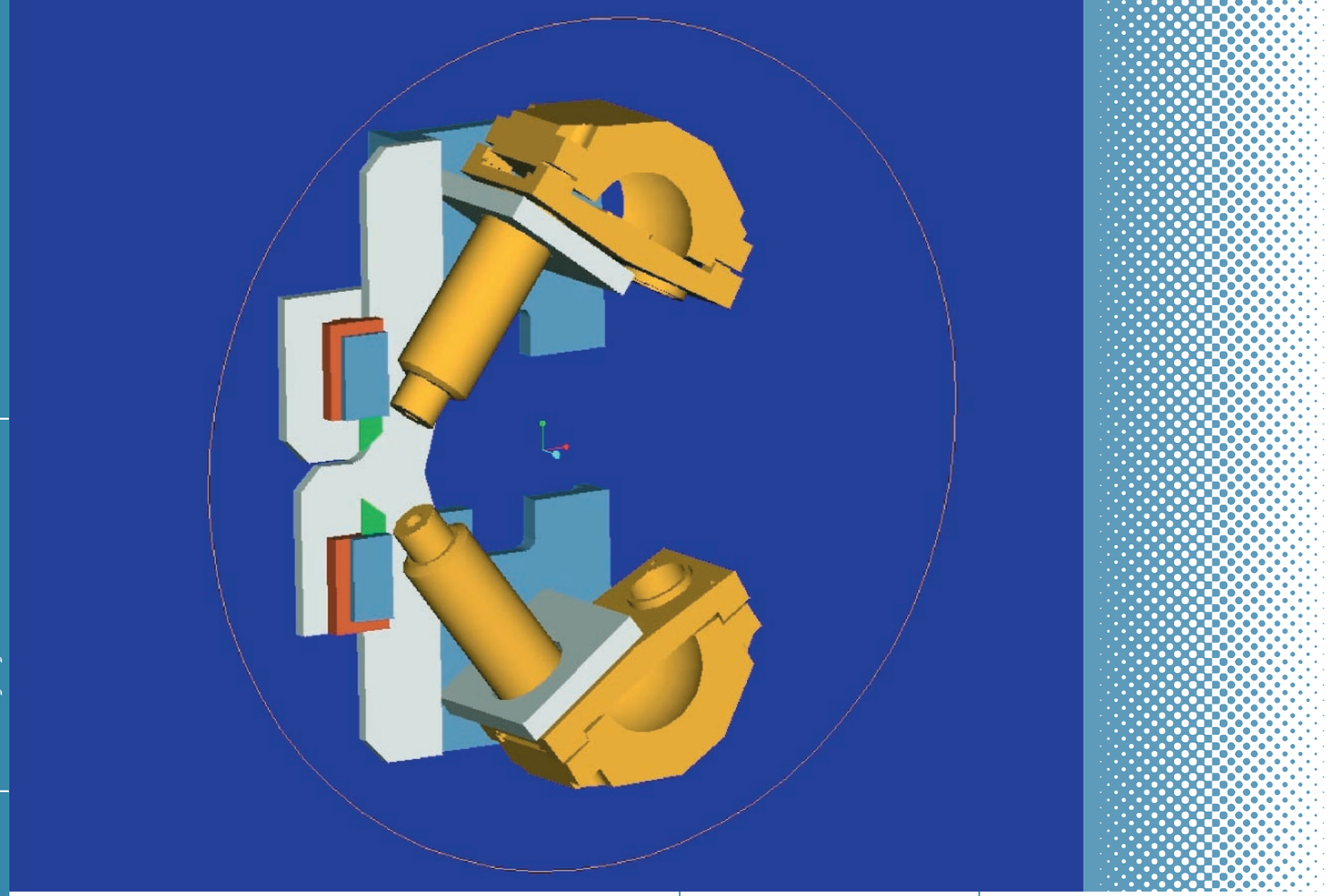

FIGURE 14

The New pBPM prototype layout showing intercepting blades and electron energy analysers. The photon beam enters from the right.

A major limitation to the continuing improvement of the performance of ELETTRA is the fact that the beam has to be injected at 1.0 GeV and ramped to 2.0 GeV. Despite the operational improvements to reduce the injection time to a minimum there are still a number of important consequences of the present arrangement. The first is that the possibility of implementing insertion devices with smaller gaps is severely compromised since such gaps imply a reduced lifetime, necessitating more frequent injection and therefore a greater percentage of time lost. In addition there is a major limitation to the stability of the closed orbit because of the thermal cycling that occurs during refills. Injection at full-energy opens the possibility of regular or top-up injection in order to maintain constant thermal conditions. In addition, if this can be achieved with undulators closed and beam shutters open, the thermal load on optical elements is also kept constant.

The two options were studied for upgrading the injection system that were compatible with the maximum envisaged storage ring operational energy (~2.5 GeV) in addition to the possibility of performing a top-up injection. These were an upgrade to the linac injector, by means of a recycling scheme, and a booster synchrotron. Following a review by an independent team of experts a decision was taken to concentrate on a study of a booster synchrotron which could be conveniently located in the open space on the inside of the storage ring building. Leaving allowance for shielding etc., a machine with a maximum radius of around 25 m can be accommodated, which allows an energy of 2.5 GeV to be comfortably reached. Construction can be performed without major interference to the operation of the light source, up to the moment of connection. A design study will be carried out in 1999.

External Contracts

The year saw also intense activity in the design and building of machine components for other laboratories. In particular the construction of two wigglers for CLRC (Darebury, UK) was successfully concluded. The work order for the construction of the ANKA (Karlsruhe, Germany) radio frequency system is well underway. The first cavity passed the acceptance tests and has been delivered. To increase the efficiency of the conditioning of the cavities an automatic system with feedback was designed to perform the task. The order for the construction of the radio frequency system for the Swiss Light Source was won and the initiated work will cover a period of 34 months. Furthermore work initiated on the fabrication of an ELETTRA type cavity for Brazilian light source in Campinas.